Nano Research

Open Access

Research Article

A bionic strong and tough amphibious adhesive inspired by barnacles and articular cartilage

Wei Tian[1,3], Jiajia Deng[1], Jing Zheng[1] ✉, and Zhongrong Zhou[1,2]

[1] *Tribology Research Institute, School of Mechanical Engineering, Southwest Jiaotong University, Chengdu 610031, China*
[2] *Macao Polytechnic University, Macao 999078, China*
[3] *Weihai Institute for Bionics, Jilin University, Weihai 264207, China*

Cite this article: *Nano Research*, **2027**, *20*, 94909211. https://doi.org/10.26599/NR.2026.94909211

ABSTRACT: Developing strong and tough amphibious adhesives that can achieve high adhesion strength in both dry and wet environments remains a major challenge. Herein, inspired by the hydrophobic–hydrophilic adhesion strategy of barnacle cement proteins and the fibre-reinforced load-bearing structure of articular cartilage, a bioinspired polyurethane adhesive (TA@WS_2/PU) with strong, tough, and durable underwater adhesion was developed. In this system, catechol-containing chain extenders were introduced to provide robust substrate anchoring, while fluorinated polyimide segments induced pronounced microphase separation and generated low-surface-energy hydrophobic nanodomains for interfacial dewetting. Furthermore, tannic-acid-modified tungsten disulfide nanosheets (TA@WS_2) were incorporated into the optimized polyurethane matrix to construct a cartilage-mimetic reinforcing network, in which high-aspect-ratio nanosheets acted as load-bearing skeletons and tannic-acid-rich surfaces formed dense hydrogen-bonding interactions with polyurethane chains. The resulting 10%-TA@WS_2/PU adhesive (the addition of TA@WS_2 is 10 wt.%) exhibited a tensile strength of 108 MPa, elongation at break of 1150%, and toughness of 371 MJ·m^{-3}, together with a dry lap-shear strength of 9.6 MPa on Fe substrates. More importantly, it achieved an underwater lap-shear strength of 4.2 MPa and maintained excellent interfacial stability during prolonged aqueous exposure. Multiscale analyses across molecular, microscopic, and macroscopic scales revealed that the superior underwater adhesion originated from the cooperative effects of hydration-layer disruption, exposed adhesive groups, compact microphase-separated packing, and nanosheet-induced diffusion barriers. This dual-bioinspired strategy provides a promising route for developing strong, tough, durable, and recyclable amphibious adhesives.

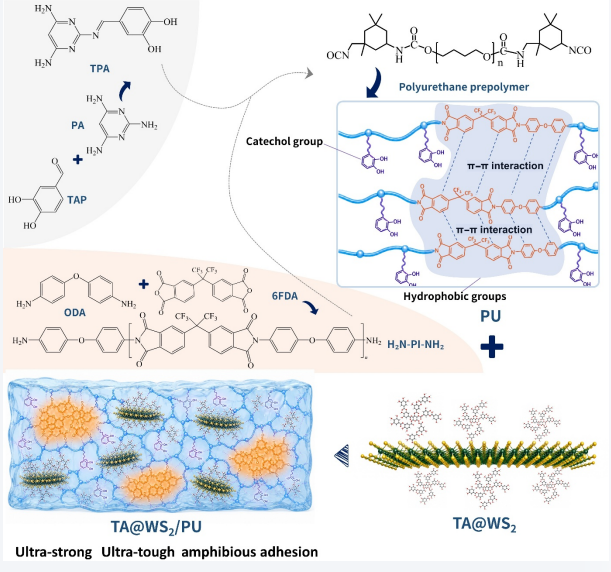

KEYWORDS: bionic adhesive, polyurethane, amphibious adhesive, high strength and high toughness

1 Introduction

Adhesives have become indispensable materials ranging from everyday products to high-end technological applications [1–3]. The global adhesive market consumed approximately 25–26 million tons in 2022–2023. However, conventional adhesives typically exhibit optimal bonding performance only on dry solid surfaces, which substantially limits their applications in wet or underwater environments. This limitation has stimulated growing interest in amphibious adhesives, which are capable of maintaining reliable adhesion under both dry and underwater conditions. These adhesives may be used for wet-surface maintenance, underwater sealing, bonding of structures exposed to water, and other applications involving aqueous environments [4–7]. Consequently, the development of amphibious adhesives capable of achieving strong adhesion under both dry and underwater conditions has become a current research hotspot [8–10]. Compared with

Received: July 1, 2026; **Revised:** August 27, 2026
Accepted: September 23, 2026

✉Address correspondence to jzheng168@home.swjtu.edu.cn

adhesion in air, underwater adhesion is intrinsically more demanding. The hydration layer on substrate surfaces blocks intimate molecular contact and thereby weakens interfacial interactions, whereas water ingress into the adhesive bulk disrupts intermolecular associations, promotes plasticization and swelling, and ultimately compromises cohesive integrity [11–14]. Mussel-inspired adhesives have received the earliest and broadest attention. Catechol moieties in mussel foot proteins mediate strong interfacial anchoring through hydrogen bonding, metal coordination, and π–π interactions, inspiring catechol-functionalized polymers, polydopamine coatings, and a wide range of mussel-mimetic adhesives [15–18]. Yet catechol-mediated adhesion remains readily screened by residual interfacial water and persistent hydration layers, which limits its effectiveness under practical underwater conditions [19, 20]. Thus, the core challenge for amphibious adhesives to achieve underwater adhesion lies not only in establishing robust interfacial anchoring but also in achieving efficient interfacial dehydration [21, 22].

Barnacles provide a distinct model for addressing this challenge. These marine organisms adhere firmly to rocks, ship hulls, and even other marine animals under harsh underwater conditions, and their remarkable adhesion derives from barnacle cement proteins [23, 24]. In these proteins, hydrophobic amino acids such as valine, leucine, and alanine help reduce water interference and disrupt the hydration layer, whereas hydrophilic amino acids such as glutamic acid, lysine, and aspartic acid promote strong adhesion through dense hydrogen-bonding interactions (Fig. 1(a)) [19]. This hydrophobic–hydrophilic synergy has inspired a series of barnacle-inspired underwater adhesives. Bao et al. reported a linear polymer integrating hydrophobic perfluoropolyether (PFPE) and urethane linkages, which achieved an underwater adhesion strength of 0.26 MPa [25]. Cui et al. developed dynamic hydrophobic hydrogels via micellar copolymerization and obtained an adhesion strength of 0.2 MPa [26], highlighting the role of hydrophobic interactions between long aliphatic chains and substrates. More recently, Zhang et al. designed a barnacle-inspired adhesive by incorporating bulky hydrophobic side chains into a polymer network [19]; this material exhibited an immediate underwater adhesion strength of 0.39 MPa, which increased to 1.62 MPa after about 24 h. Despite these advances, in many existing barnacle-inspired systems hydrophobic motifs are still introduced primarily as small side-chain molecules or discretely dispersed hydrophobic groups, which generate only limited low-surface-energy regions and therefore remain suboptimal for interfacial dehydration. Recent studies further suggest that, compared with isolated hydrophobic moieties, hydrophobic nanodomains or nanoclusters capable of forming localized yet quasi-continuous low-surface-energy regions at or near the interface are more effective in persistently disrupting stable hydration layers and suppressing water-induced failure. For example, periodic dynamic PFPE polymers with a hydrophobic nanophase-separated morphology exhibited an underwater adhesion strength of 0.26 MPa [25], whereas the adhesive system reported by Gao et al. employed hydrogen-bond-cross-linked hydrophobic nanodomains to achieve an underwater adhesion strength of 5.2 MPa on iron [20]. Consequently, the creation of hydrophobic domains within the polymer that exhibit continuity and scale effects is key to enhancing water removal at the underwater interface.

Meanwhile, adhesives intended for practical use must also possess high strength and toughness. For applications involving mechanical loading, impact, cyclic deformation, or prolonged immersion, brittle failure may still occur if the adhesive bulk lacks adequate strength and energy-dissipation capability. In this regard, cartilage provides a compelling biological model [27]. Human cartilage tissue consists of collagen fibers and an extracellular matrix. In the cartilage matrix, the side chains of proteoglycan molecules are connected to collagen fibrils through hydrogen bonding, forming a network structure, while large numbers of collagen fibrils are interwoven to sustain high mechanical loads (Fig. 1(c)) [28]. As a result, this hierarchical architecture, reinforced by strong supramolecular interactions, endows cartilage with both high strength and high toughness. Inspired by the microstructure of cartilage, the energy-dissipation pathways of polymer adhesives can be deliberately engineered to optimize the balance between fracture toughness and mechanical strength, thereby suppressing brittle failure. Thus, coupling efficient interfacial dehydration with cartilage-inspired toughening offers a promising route toward high-performance amphibious adhesives.

Guided by the hydrophobic–hydrophilic synergy of barnacle cement proteins and the microstructure of cartilage, we designed and fabricated a bioinspired polyurethane adhesive that exhibits stable underwater adhesion, high strength, and high toughness. First, inspired by the adhesion mechanism of barnacle cement proteins, hydrophilic catechol moieties were grafted onto the polyurethane chains to enhance interfacial anchoring. Meanwhile, a hydrophobic polyimide was introduced as a chain extender to induce pronounced microphase separation within the polyurethane matrix through π–π interactions, thereby promoting the expansion of hydrophobic domains (Fig. 1(b)). As a result, more continuous low-surface-energy regions were established at the adhesive/substrate interface, improving the ability of the adhesive to disrupt the hydration layer and achieve interfacial dewatering. To further enhance the strength and toughness of the adhesive, tannic acid-modified tungsten disulfide nanosheets ($TA@WS_2$) were incorporated into the polymer matrix to prepare a bionic adhesive ($TA@WS_2$/PU). In this system, the $TA@WS_2$ mimics the collagen fiber network found in cartilage tissue to achieve high strength and high toughness. Furthermore, the $TA@WS_2$ and the polymer matrix are tightly bound together via a dense network of hydrogen bonds; when the material undergoes deformation, mechanisms such as interfacial sliding, crack deflection, crack bridging, and stress transfer facilitate energy dissipation, thereby effectively improving the toughness of the adhesive. In addition, the presence of rigid aromatic rings and imide heterocycles imparts excellent thermal and hydrothermal stability. This dual-bioinspired design therefore offers a viable strategy for the development of robust, durable, and multifunctional adhesive materials.

2 Results and discussion

2.1 Synthesis and characterization of polyurethane (PU) matrix

The synthetic route of PU is presented in Fig. 1(b), and includes the synthesis of catechol-grafted functional chain extender (TPA), amino-terminated fluorinated polyimide chain extender (H_2N-PI-NH_2), polyurethane prepolymer, and their copolymerization (the details are described in the Electronic Supplementary Material (ESM)). The TPA was synthesized via a Schiff-base condensation reaction between 2,4,6-triaminopyrimidine (PA) and

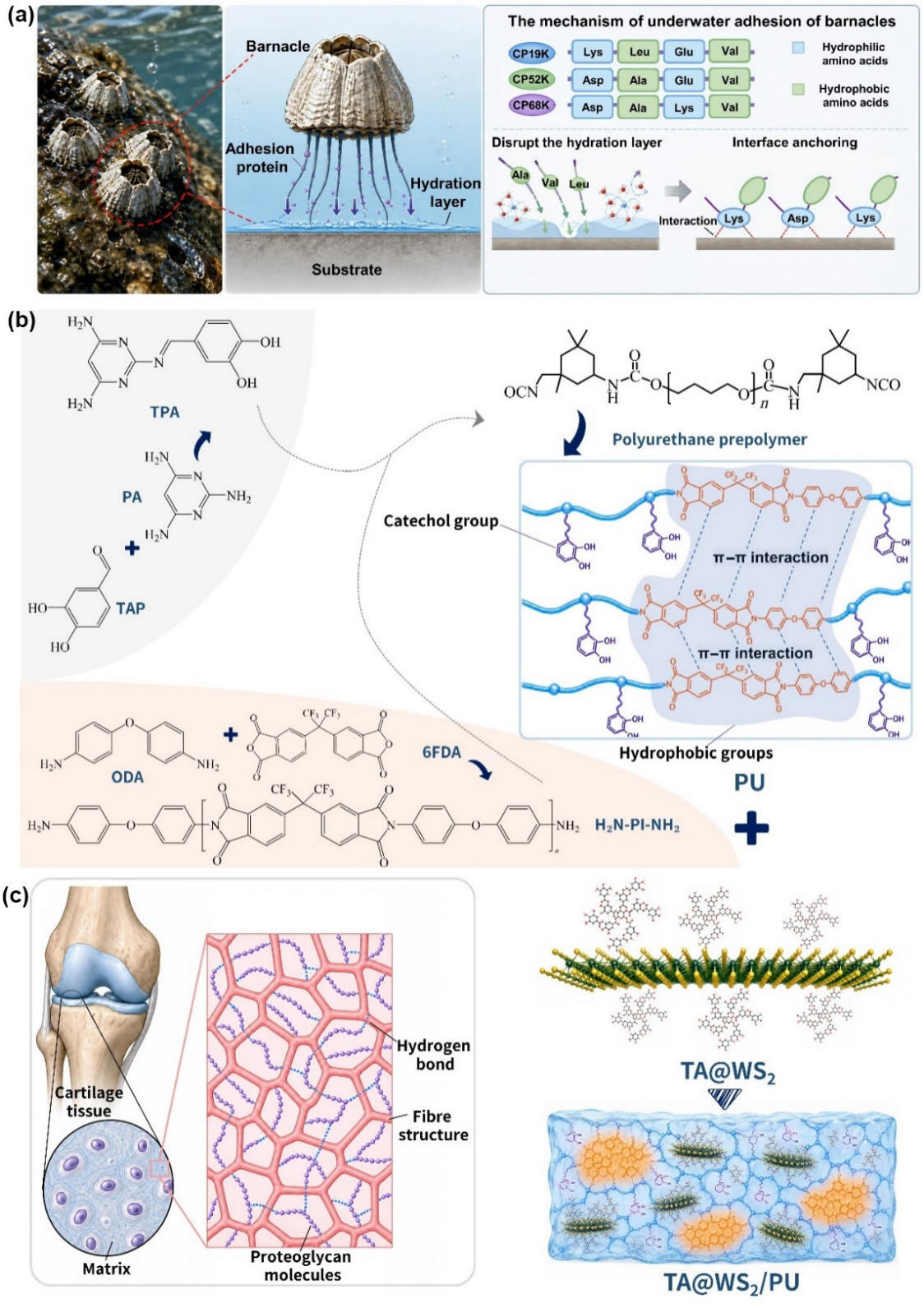

Figure 1 (a) The underwater adhesion mechanism of barnacles. (b) Preparation process of PU and TA@WS_2/PU. (c) Schematic illustration of a cartilage structure.

protocatechualdehyde (TAP). The successful formation of TPA was confirmed by Fourier transform infrared spectroscopy (FT-IR) and nuclear magnetic resonance (NMR) analyses. In the FT-IR spectrum (Fig. S1 in the ESM), the characteristic absorption band at 1642 cm^{-1} was assigned to the stretching vibration of the imine bond, indicating the formation of the Schiff-base linkage. Meanwhile, the aldehyde-related signals markedly disappeared, suggesting the consumption of the aldehyde precursor. Consistently, in the NMR spectrum (Fig. S2 in the ESM), the disappearance of the aldehyde carbon resonance in the 190–195 ppm

region, together with the appearance of an imine carbon signal at 162 ppm [20], further verified the successful synthesis of TPA. The H_2N-PI-NH_2 was prepared through the polyaddition reaction of 4,4'-oxydianiline (ODA) and 4,4'-(hexafluoroisopropylidene) diphthalic anhydride (6FDA), followed by thermal imidization. Through adjusting the molar ratio of ODA to 6FDA, the molecular weight of H_2N-PI-NH_2 could be controlled. Herein, the molar ratios of 6FDA to ODA were set at 1:1.2, 1:1.4, 1:1.6, 1:1.8, and 1:2.0. As shown in Fig. S3 in the ESM, the strong absorption bands at 1782 and 1718 cm^{-1} are assigned to the asymmetric and symmetric stretching vibrations of the imide carbonyl groups, respectively. The band at 1373 cm^{-1} corresponds to the C–N stretching vibration of the imide ring. These results clearly demonstrate the successful synthesis of H_2N-PI-NH_2. The polyurethane prepolymer was prepared according to our team's previous work via the addition reaction of isophorone diisocyanate (IPDI) and polytetrahydrofuran (PTMG). Finally, TPA and H_2N-PI-NH_2 were then co-introduced into the polyurethane prepolymer to construct a series of PU containing catechol groups and fluorinated polyimide groups (Fig. 1(b)). According to the different 6FDA/ODA molar ratios, the resulting samples were designated as PU1.2, PU1.4, PU1.6, PU1.8, and PU2.0, respectively. The FT-IR spectra of the obtained PU samples confirmed the successful formation of the target polymer (Fig. 2(a)). The strong absorption band at 1724 cm^{-1} was assigned to the stretching vibration of the carbonyl group in urethane linkages (–NHCOO–) [29], while the band at 1546 cm^{-1} corresponded to the N–H bending and C–N stretching vibrations, both characteristic of urethane bonds [30]. The absorptions at 1100 and 1241 cm^{-1} were attributed mainly to the stretching vibrations of C–O–C and C–N groups [31], further evidencing the formation of the polyurethane framework. Overall, these results demonstrate that PU samples were successfully synthesized.

To endow PU with excellent underwater adhesion, we deliberately reinforced its microphase-separated morphology of hydrophobic regions. This structural feature is not merely a morphological refinement but a prerequisite for maintaining adhesive performance under harsh hot-wet and submerged conditions. The evolution of microphase separation in the PU was interrogated by X-ray diffraction (XRD). XRD patterns show a broad diffraction peak centered at $2\theta \approx 20°$ without discernible sharp reflections (Fig. 2(b)), indicating that all samples remain predominantly noncrystalline [32]. Notably, as the polyimide chain length increases, the diffraction band becomes more intense, implying enhanced local segmental packing and structural correlation. This interpretation is consistent with atomic force microscopy (AFM) observations (Fig. 2(c)), which reveal progressively clearer nanoscale phase contrast and increasingly distinct domain features as the molecular chain length of H_2N-PI-NH_2 increases. In contrast to the blurred boundary observed at lower chain length of H_2N-PI-NH_2, PU1.2, PU1.4, and PU1.6 exhibit more pronounced nanoscale heterogeneity, indicative of stronger segregation between rigid hard domains and soft domains. Small angle X-ray scattering (SAXS) provides more direct evidence for this structural evolution because it is highly sensitive to nanoscale compositional fluctuations and domain formation. With increasing molecular weight of H_2N-PI-NH_2, the one-dimensional (1D) SAXS profiles display progressively sharper and more intense interference peaks, while the two-dimensional (2D) patterns evolve from diffuse rings to well-defined halos (Figs. 2(d) and 2(e)). These results collectively indicate a gradual enhancement of microphase separation with increasing polyimide chain length. Taken together, the above results consistently demonstrate that extending the fluorinated polyimide segment promotes the formation of better-defined hard domains and a more organized microphase-separated nanostructure. To further elucidate the molecular origin of this behavior, density functional theory (DFT) calculations were performed on representative H_2N-PI-NH_2 segments. Calculations of the average local ionisation energy (ALIE) indicate that significantly low ALIE values are observed directly above and below the plane of the benzene ring, whilst high ALIE values are observed at the ring periphery and on the outer side of the C–H bonds (Fig. 2(f)). This distribution suggests that the delocalised π electrons of the benzene ring are highly susceptible to polarisation or removal, enabling them to act as effective electron donors in π–π stacking. Furthermore, the interaction region indicator (IRI) calculations reveal distinct intermolecular interactions between polyimide chains, suggesting that aromatic imide groups possess an inherent tendency towards self-assembly (Fig. 2(g)). Such interactions provide the driving force for the local enrichment and aggregation of rigid segments upon incorporation into the PU. Molecular dynamics (MD) simulations directly visualize pronounced hard-segment aggregation in the PU samples (Fig. S4 in the ESM), confirming that the fluorinated polyimide segments are not randomly dispersed but preferentially assemble into localized hard-domain regions. More importantly, the cohesive energy density increases monotonically with increasing polyimide chain length (Fig. S5 in the ESM), whilst the intermolecular free volume fraction decreases (Fig. S6 in the ESM). This indicates progressively stronger intermolecular cohesion and more stable domain packing. This energetic trend provides a direct molecular-level explanation for the experimental observations: Enhanced intermolecular attraction promotes hard-segment association, suppresses hard/soft mixing, and thereby amplifies the extent of microphase separation.

The tensile properties of the PU samples show a pronounced nonmonotonic dependence on the molecular weight of H_2N-PI-NH_2, in good agreement with the evolution of their microphase-separated nanostructure. As shown in Fig. 2(h), all samples maintain tensile strengths of 50–75 MPa. Among them, PU1.4 exhibits the best overall mechanical performance, delivering the highest tensile strength (74 MPa) and toughness (259 $MJ \cdot m^{-3}$) (Figs. 2(h) and 2(i)). Its excellent load-bearing capability is further demonstrated by a 0.5 g specimen supporting a 10 kg weight (Fig. S7 in the ESM). Its true fracture stress reaches 0.74 GPa (Fig. S8 in the ESM), close to that of typical spider silk (0.8–1.5 GPa). In contrast, further increasing the polyimide chain length leads to a decline in tensile strength and toughness. Combined with the AFM and SAXS results, these data indicate that the mechanical performance is dictated by the extent of hard/soft phase organization. At an appropriate chain length, the fluorinated polyimide segments form cohesive yet deformable hard nanodomains that act as efficient physical cross-linking sites, enabling effective stress transfer while preserving soft-phase deformability. This optimized nanophase morphology promotes cooperative deformation and energy dissipation during stretching, whereas excessive hard-domain association and overly strong phase segregation restrict segmental mobility and accelerate strain localization. The superior strength–toughness combination of PU1.4 therefore arises from an optimal balance between hard-domain cohesion and soft-segment deformability. The cyclic tensile behavior of PU1.4 further highlights the functional role of its

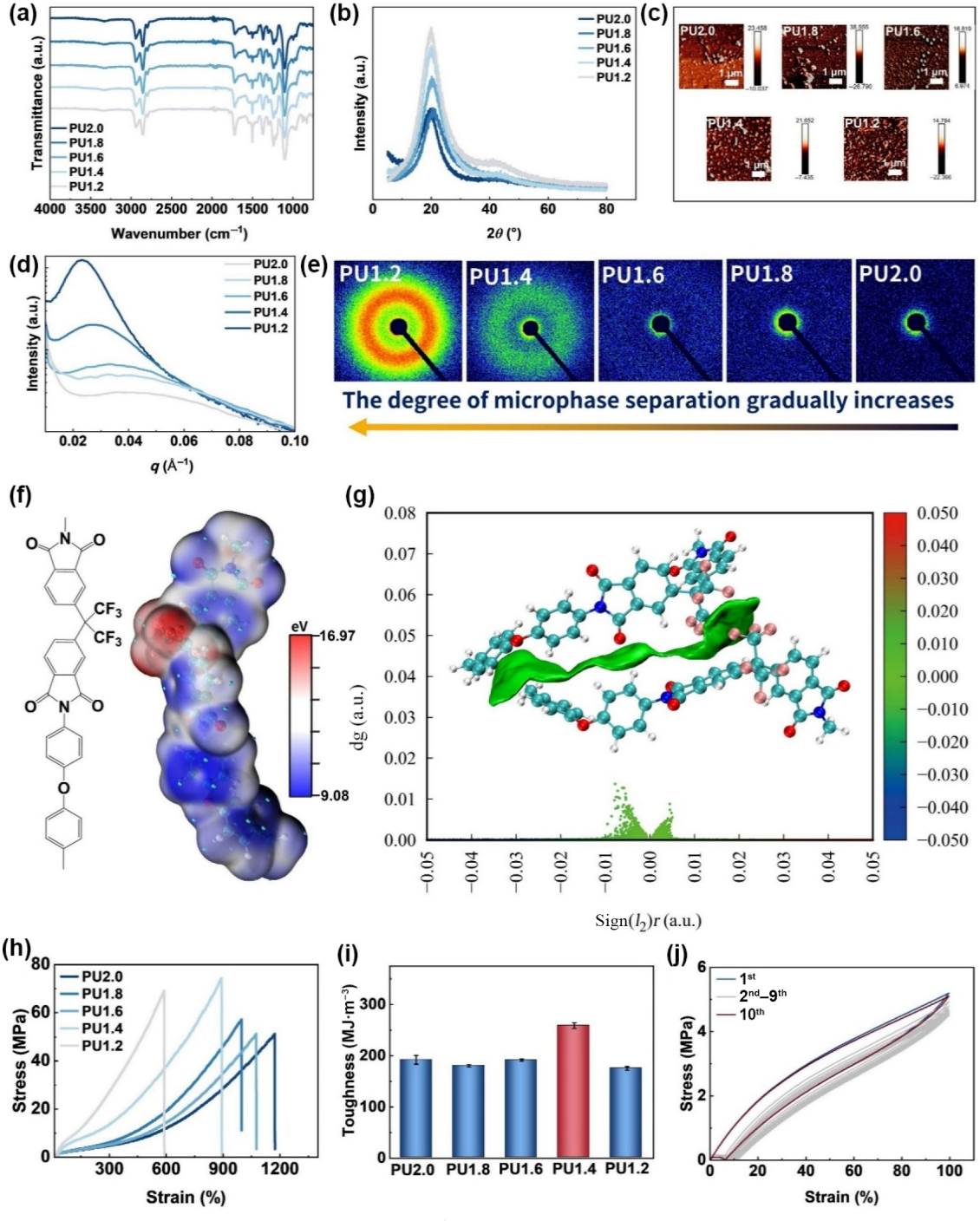

Figure 2 (a) FT-IR, (b) XRD, (c) AFM, (d) SAXS (1D), (e) SAXS (2D), (f) average local ionisation energy, (g) interaction region indicator, (h) stress–strain, and (i) toughness of PU. (j) Tensile cycle curve of PU1.4.

optimized microphase-separated structure. As shown in Fig. 2(j), PU1.4 maintains stable cyclic deformation over the first nine consecutive cycles, with only ≈ 6.8% residual strain in the second cycle. After 2 h of recovery, the 10th cycle nearly overlaps with the first, indicating efficient structural reconstruction after unloading. These results show that the optimized nanophase architecture of PU1.4 not only provides robust load-bearing hard domains, but also enables dynamic structural rearrangement, thereby endowing the material with a desirable combination of strength, toughness, elasticity, and recoverability.

This hydrophobic microphase-separated structure also enhances the water and corrosive medium resistance of materials. After immersion in water, HCl solution (pH = 5), and NaOH solution (pH = 9) for 7 days, the tensile strength of PU1.4 decreases by 17.6%, 16%, and 20%, respectively. In contrast, the control group (polyurethane containing only TPA without fluorinated polyimide segments) exhibited significant attenuation (Figs. S9(a) and S9(b) in the ESM). This enhanced aqueous durability originates from its optimized microphase-separated nanostructure. The fluorinated polyimide-rich hard nanodomains reduce local water affinity (Fig.

S10 in the ESM), disrupt hydrophilic transport pathways, and, together with the more cohesive nanophase packing, impede water ingress into the bulk. Consistently, the FT-IR spectra remain essentially unchanged after immersion in water, HCl solution (pH = 5), and NaOH solution (pH = 9) (Fig. S11 in the ESM), confirming the chemical stability of the polymer backbone. These results demonstrate that the outstanding water resistance of PU1.4 arises from the combination of interfacial water repellency, hindered bulk diffusion, and a robust microphase-separated nanostructure. PU1.4 also exhibited enhanced thermal robustness. Thermogravimetry analysis (TGA) shows that all PU samples follow a similar thermal decomposition pathway but display discernible differences in decomposition temperature (Fig. S12 in the ESM), underscoring the important role of fluorinated polyimide segment length in determining thermal stability. This improved thermal robustness originates from the incorporation of fluorinated polyimide segments, whose rigid backbone and strong intermolecular interactions enhance conformational stability and retard thermally induced structural deterioration. Consistent with this trend, PU1.4 shows much better thermomechanical stability than the control group containing only TPA (Figs. S13(a) and S13(b) in the ESM). Although both samples undergo mechanical attenuation with increasing temperature, the stress–strain response of PU1.4 changes much less markedly, indicating a more stable load-bearing network under heating. Together, these results indicate that the optimized microphase-separated nanostructure of PU1.4 effectively resists thermal perturbation, thereby enabling durable mechanical performance at elevated temperature.

2.2 Synthesis and characterization of TA@WS_2 and TA@WS_2/PU

TA@WS_2 was prepared via a TA-assisted exfoliation strategy (the details are described in the ESM). This design takes advantage of the unique molecular structure of TA, which contains multiple aromatic rings and abundant phenolic hydroxyl groups. The aromatic domains of TA exhibit strong affinity toward the basal plane of layered WS_2 through noncovalent interactions, enabling rapid adsorption onto newly exposed WS_2 surfaces during sonication. Meanwhile, the hydroxyl-rich outer surface of TA stabilizes the exfoliated nanosheets in dispersion and suppresses their restacking. The morphology of the obtained TA@WS_2 nanosheets was first examined by transmission electron microscopy (TEM). As shown in Fig. 3(a), TA@WS_2 displayed highly transparent, wrinkled, and laterally extended nanosheets with a uniform distribution of oxygen, sulphur, and tungsten. The TEM image revealed the absence of obvious thick aggregates and instead showed well-dispersed sheet-like features, indicating efficient delamination during the TA-assisted exfoliation process. AFM measurements further revealed that the TA@WS_2 nanosheets exhibited a thickness mainly ranging from 6.5 to 7.38 nm, with a representative thickness of approximately 7.21 nm (Fig. S14 in the ESM), further confirming their ultrathin morphology. This ultrathin high-aspect-ratio morphology is structurally important because it maximizes the interfacial area exposed to the surrounding polymer matrix and provides a geometric basis for the formation of a percolated reinforcing framework. Raman spectroscopy provided additional evidence for the exfoliation-induced structural evolution of WS_2. As shown in Fig. 3(b), WS_2 displayed the characteristic peak at 353.3 and 418.0 cm^{-1}, respectively. After TA-assisted exfoliation, these two modes shifted to 356.7 and 420.1 cm^{-1}, and the frequency difference between them decreased from 64.7 to 63.4 cm^{-1}, indicating reduced interlayer coupling and a decreased layer number. Meanwhile, the Raman peaks of TA@WS_2 remained sharp and well defined, suggesting that the exfoliation process largely preserved the intrinsic crystalline framework of WS_2 rather than inducing severe lattice disorder. The successful surface functionalization of WS_2 by TA was further confirmed by FT-IR and XRD analyses. In the FT-IR spectra (Fig. 3(c)), for WS_2, an –OH absorption peak attributed to adsorbed water appears at 3460 and 1630 cm^{-1}, with no other distinct characteristic peaks. TA exhibits characteristic absorptions at 3460 cm^{-1} (–OH), 1451 cm^{-1} (C=C), and 1322 cm^{-1} (C–OH). After modification, TA@WS_2 shows new characteristic peaks near 1451 and 1322 cm^{-1} corresponding to aromatic rings and C–OH, indicating that TA has been successfully loaded onto the surface of WS_2 nanosheets. XRD analysis provided complementary structural evidence (Fig. 3(d)). WS_2 exhibited the typical reflections of layered 2H-WS_2 at 14.3°, 28.9°, 32.7°, 33.5°, 39.6°, 43.9°, 49.8°, 58.4°, and 60.5° corresponding to the (002), (004), (100), (101), (103), (006), (105), (110), and (008) planes, respectively. After TA-assisted exfoliation, TA@WS_2 exhibits weakened diffraction peaks, which is attributed to the adsorption of TA onto the surface of the WS_2 nanosheets, thereby disrupting the periodic arrangement of the surface lattice. XPS analysis further verified the hybrid nature of TA@WS_2 and provided insight into the interfacial electronic interaction between TA and WS_2. As shown in Fig. 3(e), WS_2 exhibited the characteristic W 4f peaks at 33 eV, together with the corresponding S 2p peaks at 163.6 eV. In TA@WS_2, these W- and S-related peaks were retained (the peaks intensity are relatively weak), confirming the preservation of the WS_2 framework, while their slight shifts of approximately 0.3 eV indicated an interfacial electronic interaction between TA and WS_2. More importantly, the C 1s and O 1s signals were significantly enhanced in TA@WS_2. The high-resolution C 1s spectrum could be deconvoluted into components at 284.8, 286.2, and 288.5 eV, assigned to C–C, C–O, and C=O species (Fig. S15(a) in the ESM), respectively, while the O 1s spectrum showed peaks at 531.7 and 533.2 eV corresponding to carbonyl-/ether- and hydroxyl-containing oxygen species (Fig. S15(b) in the ESM). These results collectively confirm that TA was successfully anchored onto the WS_2 surface during exfoliation, producing a hybrid nanostructure with a rigid inorganic core and a polyphenol-rich shell. TGA and water-contact-angle measurements further supported this conclusion. As shown in Fig. 3(f), WS_2 exhibited excellent thermal stability and retained 99 wt.% of its mass at 800 °C, whereas TA showed substantial degradation in the range of 200–330 °C and a final residue of only 18.4 wt.%. TA@WS_2 displayed an intermediate behavior, with a characteristic additional weight-loss step in the same degradation region and a residual mass of 37 wt.% at 800 °C. On the basis of the residual-mass analysis, the TA content in TA@WS_2 was estimated to be 43.6 wt.%, confirming that a considerable amount of TA was immobilized on the nanosheet surface. Correspondingly, the water contact angle decreased from 74.6° for WS_2 to 48.6° for TA@WS_2 (Fig. S16 in the ESM), indicating that TA functionalization markedly improved the interfacial wettability of WS_2 by introducing abundant phenolic hydroxyl groups. This change is highly beneficial for subsequent incorporation into the polyurethane matrix because it improves dispersion and provides abundant dynamic interaction sites for hydrogen bonding with the polymer chains. To further understand the driving force underlying TA-

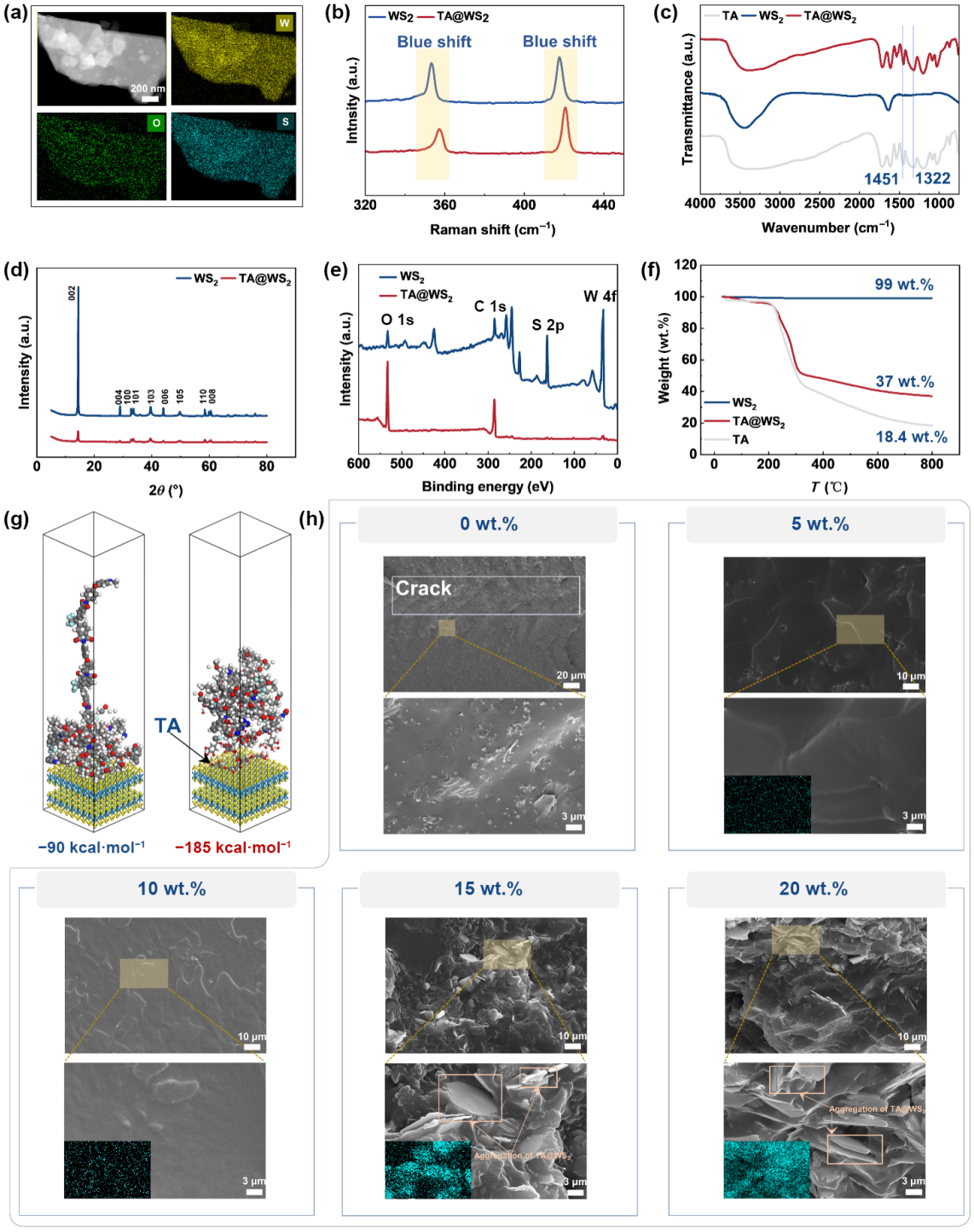

Figure 3 (a) TEM, (b) Raman, (c) FT-IR, (d) XRD, (e) XPS, and (f) TGA of WS_2 and TA@WS_2. (g) Binding energy of the PU1.4 molecular chain on WS_2 and TA@WS_2 substrates. (h) Cross-sectional views of TA@WS_2/PU.

assisted exfoliation, DFT calculations were performed to compare the interaction of TA with monolayer WS_2 and the interlayer binding between adjacent WS_2 sheets. As shown in Fig. S17 in the ESM, the calculated binding energy between neighboring WS_2 layers was −69 kcal·mol^{-1}, whereas the adsorption energy of a TA molecule on monolayer WS_2 reached −286 kcal·mol^{-1}, which is approximately 314% higher than the WS_2-WS_2 interlayer interaction. These calculations provide a molecular-level explanation for the experimental observations. Once sonication weakens the van der Waals attraction between WS_2 layers, TA can rapidly adsorb onto the freshly exposed nanosheet surface, outcompete interlayer restacking, and stabilize the exfoliated nanosheets in dispersion. In addition, the aromatic rings of TA act as an adsorption platform for WS_2, whereas the exposed phenolic hydroxyl groups remain available for subsequent interactions with the polymer matrix.

PU1.4 was selected as the polymer matrix for nanocomposite construction because it showed the best overall balance of strength,

toughness, elasticity, water resistance, and thermomechanical stability among the PU series. Its optimized microphase-separated nanostructure, featuring sufficiently cohesive yet still deformable hard domains, provides an ideal matrix for nanofiller reinforcement by enabling efficient stress transfer without sacrificing soft-phase deformability. Based on the TA-assisted exfoliation and stabilization of WS_2, a cartilage-mimetic nanocomposite, denoted TA@WS_2/PU, was subsequently constructed by incorporating TA@WS_2 nanosheets into the PU1.4 matrix. In this system, TA suppresses the restacking of WS_2 nanosheets and endows them with abundant interfacial binding sites. The zeta potential measurements showed that TA@WS_2 possessed a more negative surface potential than pristine WS_2 (Fig. S18 in the ESM), indicating enhanced electrostatic repulsion between neighboring nanosheets, which helps suppress aggregation and maintain their dispersion, while the phenolic hydroxyl and ester groups of TA promote dense hydrogen-bonding interactions with PU1.4. As a result, TA@WS_2 can be tightly integrated into the polymer network rather than simply embedded within it. This strong interfacial affinity is further supported by molecular simulation, in which the binding energy between PU and TA@WS_2 reaches −185 kcal·mol^{-1}, in sharp contrast to only −90 kcal·mol^{-1} for PU and monolayer WS_2 (Fig. 3(g)). Therefore, TA adsorption transforms WS_2 into a highly interactive nanoscale reinforcing unit capable of coupling strongly with the PU matrix. This interfacial design gives rise to a cartilage-like reinforcing architecture in the composite. Analogous to the collagen fibril network in cartilage, the high-aspect-ratio TA@WS_2 nanosheets act as nanoscopic load-bearing skeletons, whereas the TA-rich surface establishes dense noncovalent interactions with the surrounding PU1.4 matrix, thereby promoting stress transfer and energy dissipation. To more accurately evaluate the dispersion state of the synthesized TA@WS_2 in the PU1.4 matrix, the cross-sectional morphologies of TA@WS_2/PU composites containing 0 wt.%, 5 wt.%, 10 wt.%, 15 wt.%, and 20 wt.% TA@WS_2 were observed using scanning electron microscopy-energy dispersive X-ray spectroscopy (SEM-EDS) (Fig. 3(h)). At a TA@WS_2 loading of 0 wt.%, the fracture surface exhibited typical brittle fracture characteristics, accompanied by pronounced oriented cracks. With the introduction of TA@WS_2, the composite fracture surfaces gradually became rougher, indicating enhanced interfacial interaction between the filler and the polyurethane matrix. Meanwhile, the presence of TA@WS_2 effectively hindered the formation of oriented cracks and suppressed their further propagation to some extent, suggesting its beneficial role in improving the energy dissipation capability and fracture resistance of the material. However, when the TA@WS_2 content was further increased to 15 wt.% or above, local filler enrichment and a certain degree of agglomeration began to appear on the fracture surfaces, indicating that the addition of excessive nanosheets compromises the structural uniformity of the system, which is detrimental to further improvement in composite performance. Collectively, the optimal loading of TA@WS_2 is determined to be 10 wt.%. Herein, the TA@WS_2/PU sample containing 10 wt.% TA@WS_2 is designated as 10%-TA@WS_2/PU.

2.3 Mechanical properties of TA@WS_2/PU

The incorporation of TA@WS_2 markedly enhanced the tensile properties of the PU1.4 matrix. As shown in Fig. 4(a), both tensile strength and elongation at break increased with TA@WS_2 loading from 5 wt.% to 10 wt.%, indicating that TA@WS_2 simultaneously improved the load-bearing capability and deformability of the composite. PU1.4 exhibited a tensile strength of 74 MPa, an elongation at break of 890%, and a toughness of 259 MJ·m^{-3}, whereas the composite containing 10 wt.% TA@WS_2 reached 108 MPa, 1150%, and 371 MJ·m^{-3}, respectively (Figs. 4(a) and 4(b)), and exhibited excellent resilience (Fig. 4(c)). When the TA@WS_2 content was further increased to 15 wt.%, both strength and ductility decreased, although they remained higher than those of PU1.4. This nonmonotonic dependence indicates that the reinforcement effect of TA@WS_2 is governed by a balance between interfacial coupling and structural homogeneity. The superior mechanical performance at intermediate TA@WS_2 loading (5 wt.%–10 wt.%) arises from the strong structural compatibility between TA@WS_2 and PU1.4 matrix. The high-aspect-ratio TA@WS_2 nanosheets act as cartilage-like load-bearing skeletons, while the TA-rich surface forms dense hydrogen-bonding interactions with PU1.4, thereby enabling efficient stress transfer and suppressing premature interfacial failure. Meanwhile, the optimized nanophase structure of PU1.4 preserves soft-phase deformability and allows cooperative deformation of the composite under load. This structure–property relationship is further supported by tensile-mode SAXS (Fig. 4(d)). 10%-TA@WS_2/PU underwent a continuous structural evolution during tensile deformation, transitioning from an initially ordered state to a disordered intermediate state and finally to a highly oriented reconstructed state at large strain. The pronounced scattering peak at 0% strain indicates the presence of stable nanoscale correlated structures within the system. When the strain increased to 100%, the original microphase-separated domains and filler–matrix interfacial correlations were disrupted, leading to a marked weakening or even disappearance of the characteristic scattering peak. Upon further stretching, the polyurethane chains, hard-segment aggregates, and WS_2 nanosheets underwent cooperative orientation and re-established new correlated structures (Fig. 4(e)), resulting in the reappearance of the scattering peak. This phenomenon indicates that the internal structure of the material does not simply undergo progressive destruction under stress, but instead possesses a pronounced dynamic reconstruction capability. Such structural evolution is beneficial for continuously dissipating energy through interfacial sliding, reversible hydrogen-bond dissociation, chain rearrangement, and filler orientation, while simultaneously forming more efficient stress-transfer pathways at high strain, thereby enabling the synergistic enhancement of tensile strength, elongation at break, and toughness. It is worth noting that the mechanical properties of 10%-TA@WS_2/PU exceed those of most polyurethane materials (Fig. 4(f)) [33–42]. At excessive filler loading (15 wt.%–20 wt%), however, local filler-rich domains begin to appear, which reduce matrix continuity, leading to lower tensile strength and elongation at break.

The incorporation of TA@WS_2 further improved the resistance of the PU matrix to water and corrosive environments. After immersion in water, HCl solution (pH = 5), and NaOH solution (pH = 9) for 7 days, the tensile strength of 10%-TA@WS_2/PU decreases by 3%, 8.3%, and 13%, respectively, whereas PU1.4 exhibited a more noticeable reduction in mechanical performance (Fig. 4(g) and Fig. S9(a) in the ESM), demonstrating that the introduction of TA@WS_2 effectively reinforced the environmental durability of the system. This enhanced stability can be attributed to the synergistic barrier and interfacial effects introduced by the nanosheets. On the one hand, the high-aspect-ratio TA@WS_2

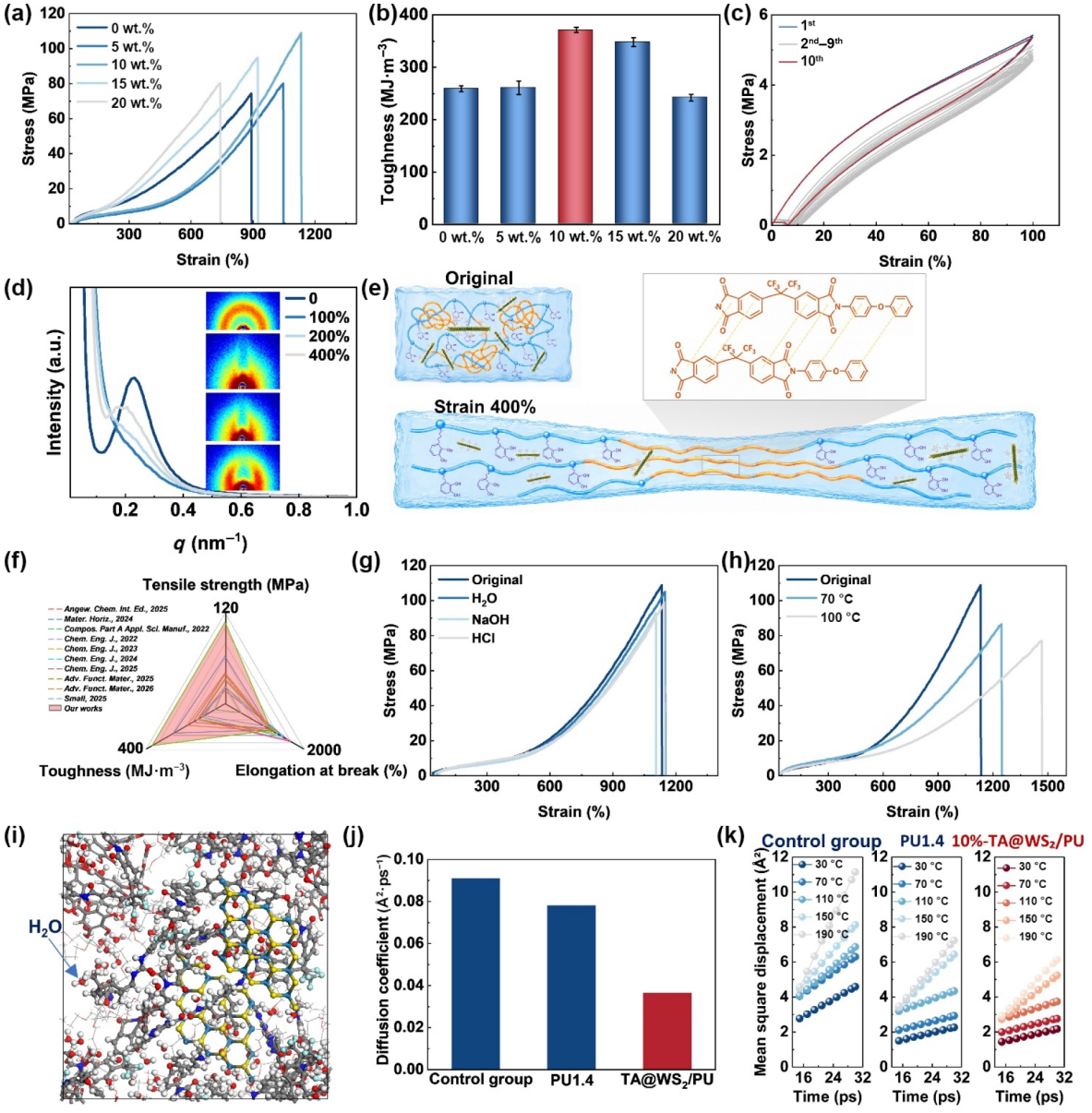

Figure 4 (a) Stress–strain and (b) toughness of TA@WS_2/PU. (c) Tensile cycle curve (perform nine consecutive stretches, then rest for two hours before performing the tenth stretch.), (d) SAXS, and (e) schematic diagram of the stretching process of 10%-TA@WS_2/PU. (f) Comparison of mechanical properties between 10%-TA@WS_2/PU and similar polyurethane types. (g) Stress–strain curves of 10%-TA@WS_2/PU after immersion in various water medium for 7 days. (h) Stress–strain curves of 10%-TA@WS_2/PU at different temperatures. (i) Kinetic diagram of water molecule diffusion in 10%-TA@WS_2/PU. (j) Diffusion coefficients for water molecules diffusing within the control group (only with TPA), PU1.4, and 10%-TA@WS_2/PU. (k) MSD of the control group (only with TPA), PU1.4, and 10%-TA@WS_2/PU.

nanosheets create a more tortuous transport pathway for water and corrosive species, thereby retarding their penetration into the bulk. On the other hand, the TA-mediated hydrogen-bonding interface strengthens matrix–filler coupling and locally immobilizes adjacent PU chains, which suppresses swelling, plasticization, and interfacial decohesion in aqueous environments. In addition, the well-dispersed nanosheets help densify the nanophase structure of the matrix and reduce the continuity of hydrophilic diffusion channels. Consistent with the above analysis, MD simulations further verified the enhanced water-barrier capability imparted by TA@WS_2. Specifically, 10%-TA@WS_2/PU exhibited a lower water diffusion coefficient than PU1.4 and the control sample (Fig. 4(j)), together with the smallest fractional free volume (Fig. S19 in the ESM), indicating that the incorporation of TA@WS_2 not only effectively suppressed water transport but also reduced the free space available for water penetration within the system. Further comparison of Fig. 4(i) and Fig. S20 in the ESM reveals that, in 10%-TA@WS_2/PU, water molecules are predominantly excluded from the regions surrounding the polyurethane hard segments and TA@WS_2 nanosheets, demonstrating a pronounced spatial exclusion effect and suggesting the formation of a denser and more selective water-resistant microstructure. By contrast, although water molecules in PU1.4 also tend to avoid the hard-segment-rich regions, their distribution remains relatively widespread throughout the system because of the absence of the additional physical barrier and interfacial confinement provided by TA@WS_2 nanosheets. In the control sample (only with TPA), water molecules are distributed almost indiscriminately throughout the entire system, indicating the

lack of an effective hydrophobic barrier and a compact nanostructure capable of restricting water ingress. These results indicate that the excellent aqueous durability of TA@WS_2/PU originates from the combined effects of nanosheet-induced diffusion blocking, strengthened interfacial cohesion, and the intrinsically robust microphase-separated PU matrix.

TA@WS_2 incorporation also promoted the thermomechanical stability of the composite. The mechanical properties of 10%-TA@WS_2/PU were tested at different temperatures. Compared with PU1.4 and the TPA-only control group, the 10%-TA@WS_2/PU composite exhibits minimal variation in stress–strain behavior upon heating, with a tensile strength of 73 MPa at 100 °C, which is significantly higher than that of PU1.4 (43 MPa) (Fig. 4(h) and Fig. S13 in the ESM), indicating that the incorporation of TA@WS_2 further enhanced the structural stability of the load-bearing network under thermal perturbation. To elucidate the underlying mechanism, molecular dynamics simulations were conducted by analyzing the mean square displacement (MSD) of the alicyclic rings in IPDI for 10%-TA@WS_2/PU, PU1.4, and the control group (only with TPA) at different temperatures (Fig. 4(k)). Although the slope of MSD of all samples increased with temperature, 10%-TA@WS_2/PU consistently showed the lowest temperature-induced increase, suggesting that TA@WS_2 effectively restricted thermally activated chain mobility. This enhanced stability can be attributed to the combined effects of the rigid two-dimensional nanosheets and the TA-mediated interfacial hydrogen-bonding interactions, which together constrain local chain motion and increase the energy barrier for segmental relaxation. Variable-temperature FT-IR spectra further supported this interpretation. In comparison with PU1.4 and the control sample, the characteristic bands of 10%-TA@WS_2/PU exhibited much smaller temperature-dependent changes (Fig. S21 in the ESM), indicating that its hydrogen-bonding network, hard-segment associations, and filler–matrix interfacial interactions remained more stable during heating. These results collectively demonstrate that TA@WS_2 further improves the thermomechanical stability of the polyurethane system by suppressing chain mobility, stabilizing the microphase-separated nanostructure, and preserving efficient stress-transfer pathways at elevated temperatures.

2.4 Dry adhesion properties of 10%-TA@WS_2/PU

To assess the dry adhesion capability of 10%-TA@WS_2/PU, lap-shear measurements were performed using Fe, Al, and Cu substrates. The obtained results demonstrate an obvious dependence of bonding strength on substrate type, with the adhesion strength decreasing in the order of Fe, Al, and Cu (Fig. 5(a)). In particular, the Fe substrate exhibited the highest lap-shear strength of 9.6 MPa. In addition to metallic substrates, 10%-TA@WS_2/PU also exhibited effective adhesion on a representative plastic substrate (Fig. S22 in the ESM), suggesting broader substrate adaptability. The strong interfacial bonding was also confirmed by the fact that the adhered joints were able to sustain the pulling force generated by a 75 kg adult as well as a vertical load of 20 kg (Fig. 5(b) and Fig. S23 in the ESM), demonstrating the excellent load-bearing capacity of the adhesive. More impressively, lap-shear samples prepared with 10%-TA@WS_2/PU were capable of overcoming the static friction of a 1.5-ton compact car and towing it forward smoothly (Movie S1 in the ESM); its lap shear strength far exceeded that of similar adhesives and commercial adhesives (Fig. 5(d)) [20, 43–55]. In contrast, replacing TPA with phenylenediamine as the chain extender led to a pronounced reduction in adhesive strength (Fig. S24 in the ESM). Meanwhile, 10%-TA@WS_2/PU exhibited a mixed failure mode, whereas the control sample (replacing TPA with phenylenediamine) was dominated by interfacial failure (Fig. S25 in the ESM), indicating that the catechol functionalities introduced by TPA markedly strengthened the interfacial bonding between the adhesive and the substrate. Furthermore, lap-shear tests using PU1.4 as a control revealed that, although the lap-shear strength of 10%-TA@WS_2/PU was only marginally higher than that of PU1.4 (Fig. 5(c)), its fracture energy on the Fe substrate was 2.2 times greater. This result suggests that 10%-TA@WS_2/PU possesses a superior energy-dissipation capability, which is expected to better sustain the stable service of bonded structures under vibration and complex loading conditions. These results reveal a clear functional distinction between interfacial adhesion and cohesive reinforcement in 10%-TA@WS_2/PU. The comparable lap-shear strengths of PU1.4 and 10%-TA@WS_2/PU indicate that TA@WS_2 does not substantially enhance the intrinsic polymer-substrate interaction, which is primarily governed by TPA and fluorinated polyimide segments. Instead, the 2.2-fold increase in fracture energy demonstrates that the principal role of TA@WS_2 is to enhance cohesive toughness and resistance to crack propagation. The high-aspect-ratio nanosheets and TA-mediated hydrogen-bonding interfaces promote stress transfer, interfacial sliding, crack deflection, and crack bridging, thereby dissipating substantially more energy during joint failure. Therefore, TA@WS_2 should be regarded primarily as a cohesive toughening and durability-enhancing component rather than an interfacial adhesion promoter.

The durability of 10%-TA@WS_2/PU under harsh environments was systematically investigated through lap-shear measurements performed after exposure to aqueous, corrosive, thermal, and hydrothermal conditions. After immersion in water, HCl solution, or NaOH solution for 24 h, the lap shear strength of 10%-TA@WS_2/PU still exceeds 7.5 MPa (Fig. 5(e)), suggesting that both the adhesive/substrate interface and the internal cohesion of the adhesive layer remained largely intact in these challenging media. Notably, even after prolonged immersion in water for 9 days, the lap-shear strength of 10%-TA@WS_2/PU decreased by only 16%, and the subsequent deterioration became extremely slow (Fig. S26 in the ESM). Furthermore, it still exhibited good durability after 28 days of immersion in water (Fig. 5(h)). When subjected to elevated temperatures, the lap-shear strength of 10%-TA@WS_2/PU gradually declined, which can be attributed to thermally induced relaxation of polymer chains. Even so, the adhesive retained more than 83% of its original strength at 100 °C (Fig. 5(f)), demonstrating excellent thermal adhesion stability. More importantly, after immersion in hot water at different temperatures for 1 day, 10%-TA@WS_2/PU still exhibited high lap-shear strength (Fig. 5(g)), confirming its strong bonding durability under combined hydrothermal conditions, which are more severe than purely aqueous or thermal exposure alone. These observations are in good agreement with the proposed structure–property relationship. Specifically, the catechol-bearing TPA segments provide robust interfacial anchoring to the substrate, helping to preserve adhesion even in wet or heated environments. Meanwhile, the fluorinated polyimide segments reduce surface wettability, suppress water permeation, strengthen microphase separation, and increase cohesive energy density, thereby mitigating swelling, thermal softening, and hydrothermal plasticization. Owing to this combination, 10%-TA@WS_2/PU is

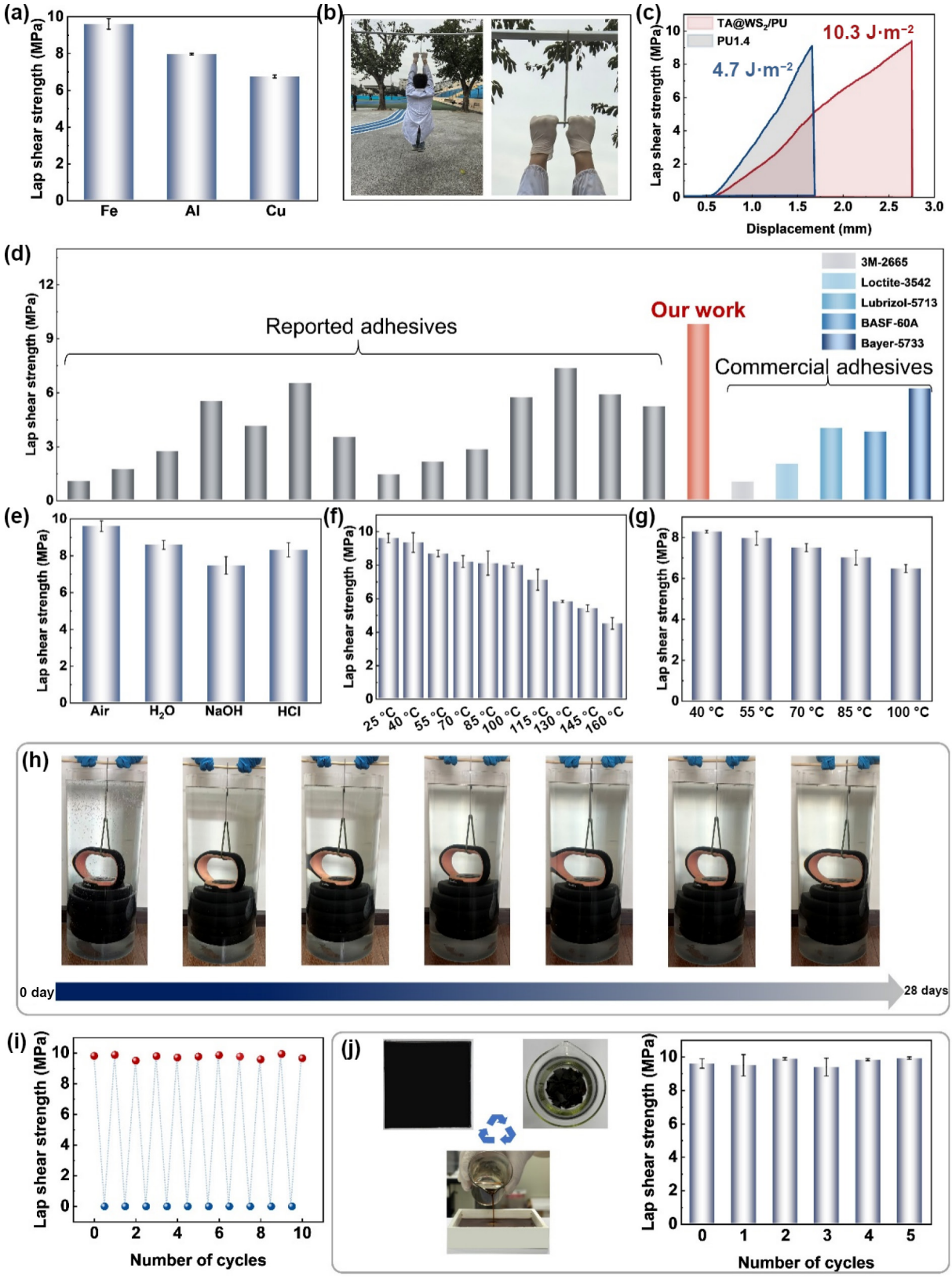

Figure 5 (a) The lap shear strength of 10%-TA@WS_2/PU on different substrates. (b) The lap shear specimen of 10%-TA@WS_2/PU can lift a 75-kg adult. (c) The shear fracture energy of 10%-TA@WS_2/PU and PU1.4. (d) Comparison of lap shear strength on Fe substrates between 10%-TA@WS_2/PU, adhesives reported, and commercial adhesives. (e) The lap shear strength of 10%-TA@WS /PU at different media. (f) The lap shear strength of 10%-TA@WS_2/PU under different temperatures. (g) The lap shear strength of 10%-TA@WS_2/PU in hot water at different temperatures. (h) Photograph of the 10%-TA@WS_2/PU sample loaded with a 10 kg object after immersion in water for 28 days. (i) The lap shear strength of 10%-TA@WS_2/PU following repeated bonding by hot-pressing. (j) The lap shear strength of 10%-TA@WS_2/PU after repeated recycling.

able to maintain both strong interfacial bonding and bulk cohesive integrity under demanding service conditions. Furthermore, TA@WS_2 effectively enhances the molecular density of 10%-TA@WS_2/PU, thereby improving its water-blocking capacity. In contrast, the control sample, which lacks the rigid fluorinated polyimide component, suffers much more severe degradation in water and at elevated temperatures (Figs. S27 and S28 in the ESM). Taken together, these findings indicate that the cooperative effect of catechol-based interfacial adhesion and fluorinated polyimide-induced network stabilization is critical for realizing durable bonding in complex environments. More broadly, the results confirm that the present molecular design not only enhances the intrinsic mechanical properties of the adhesive, but also, more importantly, enables reliable interfacial adhesion under realistic harsh service conditions. To further assess the adhesive capability of 10%-TA@WS_2/PU, pull-off tests were additionally carried out (Fig. S29 in the ESM). Notably, the trends obtained from the pull-off measurements were highly consistent with those observed in the lap-shear tests. Across different substrate types (Fig. S30 in the ESM), temperature conditions (Fig. S31 in the ESM), and environmental media (Fig. S32 in the ESM), 10%-TA@WS_2/PU consistently exhibited outstanding heat resistance, corrosion resistance, and adhesion performance. The strong agreement between these two testing methods further substantiates its multifunctional adhesive behavior, demonstrating that 10%-TA@WS_2/PU can provide reliable bonding performance under a wide range of loading and service environments.

To assess the sustainability of 10%-TA@WS_2/PU as a high-performance adhesive, its reusability and recyclability were systematically examined. After failure of the 10%-TA@WS_2/PU lap-shear joints, the fractured specimens were re-bonded by hot pressing at 160 °C under 10 MPa. Remarkably, after 10 re-bonding cycles, 10%-TA@WS_2/PU still retained over 98% of its initial lap-shear strength, evidencing excellent repeatable adhesion performance (Fig. 5(i)). This behavior indicates that thermal reprocessing can effectively reactivate the dynamic supramolecular interactions and reconstruct the microphase-separated network, thereby restoring both interfacial bonding and bulk cohesion. In parallel, 10%-TA@WS_2/PU exhibited outstanding recyclability. After dissolving the adhesive waste in N,N-dimethylformamide (DMF) at 100 °C and reprocessing it into new lap-shear samples, the material still maintained ~ 100% of its original lap-shear strength after five recycling cycles (Fig. 5(j)). To examine whether repeated dissolution caused irreversible structural deterioration, the recycled samples were further characterized by SEM and AFM (Figs. S33 and S34 in the ESM). SEM observations revealed no obvious large-scale aggregation of TA@WS_2, while AFM images showed that the characteristic nanoscale phase-separated morphology was largely preserved after recycling. These results suggest that the high recovery of adhesion arises from the reconstructability of the supramolecular and microphase-separated network. During dissolution, reversible hydrogen-bonding and hard-domain associations are temporarily disrupted; upon solvent removal, these interactions and the TA@WS_2–PU interfacial network can reorganize, thereby restoring effective load-transfer and energy-dissipation pathways. Therefore, the recycled adhesive should be regarded as structurally and functionally highly recoverable rather than molecularly identical to the pristine material. Taken together, these results show that 10%-TA@WS_2/PU unites durable adhesion with excellent reusability and recyclability, highlighting the distinctive potential of this supramolecular polyurethane system for sustainable adhesive applications. It should be emphasized that the hot-pressing and solvent-assisted recycling processes investigated here are post-service material reprocessing strategies rather than *in-situ* underwater repair procedures. The 160 °C/10 MPa treatment was employed to evaluate the structural recoverability and reprocessability of the adhesive after failure, whereas DMF-assisted dissolution was used to assess end-of-life material recycling.

To elucidate the adhesion mechanism of 10%-TA@WS_2/PU, the electrostatic potential (ESP) distributions of its representative polar moieties, including the fluorinated polyimide segment, TPA, the soft segment, and the characteristic structure of TA, were first analyzed to identify the molecular domains most likely to interact with metal substrates. Usually, the higher the electronegativity of an atom, the more readily it interacts with a metal substrate. Distinct ESP distributions were observed among these polar units; however, the electron-rich regions were predominantly localized around the O and N atoms (Figs. 6(a) and 6(b)), suggesting that these heteroatoms serve as the primary adsorption sites for interfacial interactions with metal surfaces. To further quantify their interfacial affinity, adsorption simulations of these molecular fragments on Fe(110), Al(111), and Cu(111) surfaces were carried out, and the corresponding binding energies were calculated (Fig. 6(c) and Figs. S35 and S36 in the ESM). All polar units exhibited the same substrate preference, following the order Fe > Al > Cu, in good agreement with the experimentally observed adhesion strength sequence of 10%-TA@WS_2/PU on different metal substrates. Among the four polar fragments, the binding energies decreased in the order of fluorinated polyimide segment > TPA > tannic acid moiety > soft segment, indicating that the fluorinated polyimide segment and TPA are the dominant contributors to interfacial adsorption. By contrast, although the soft segment contributes less directly to adsorption, its high chain mobility is expected to facilitate conformational adaptation and interpenetration into surface asperities, thereby promoting mechanical interlocking and enhancing overall adhesion. Molecular dynamics simulations were subsequently performed using the Forcite module in Materials Studio to further probe the interfacial binding characteristics of 10%-TA@WS_2/PU, PU1.4, and the control sample (replacing TPA with phenylenediamine) on the Fe substrate. All three systems formed stable interfaces and typically reached dynamic equilibrium within ~ 70 ps (Fig. 6(d)). Remarkably, regardless of the initial polymer configuration, the densities of N- and O-containing groups in the vicinity of the Fe surface increased substantially after equilibration (Fig. 6(e)), indicating spontaneous interfacial enrichment of polar functionalities driven by substrate-polymer interactions. This result clearly supports the migration of adsorption-active groups toward the metal surface during interfacial equilibration. In addition, the calculated interfacial interaction energies followed the order 10%-TA@WS_2/PU (~ 4163 kcal·mol^{-1}) ≈ PU1.4 (~ 4100 kcal·mol^{-1}) > control (~ 2342 kcal·mol^{-1}). The nearly identical interaction energies of 10%-TA@WS_2/PU and PU1.4 suggest that the incorporation of TA@WS_2 does not substantially alter the intrinsic polymer–Fe interfacial binding strength. This is likely because the tannic acid moieties preferentially adsorb onto the WS_2 surface and therefore contribute only minimally to direct polymer-metal adsorption, resulting in only a limited difference in adhesion strength between the two systems. In contrast, the control sample lacks catechol functionalities, such that interfacial adsorption mainly relies on the

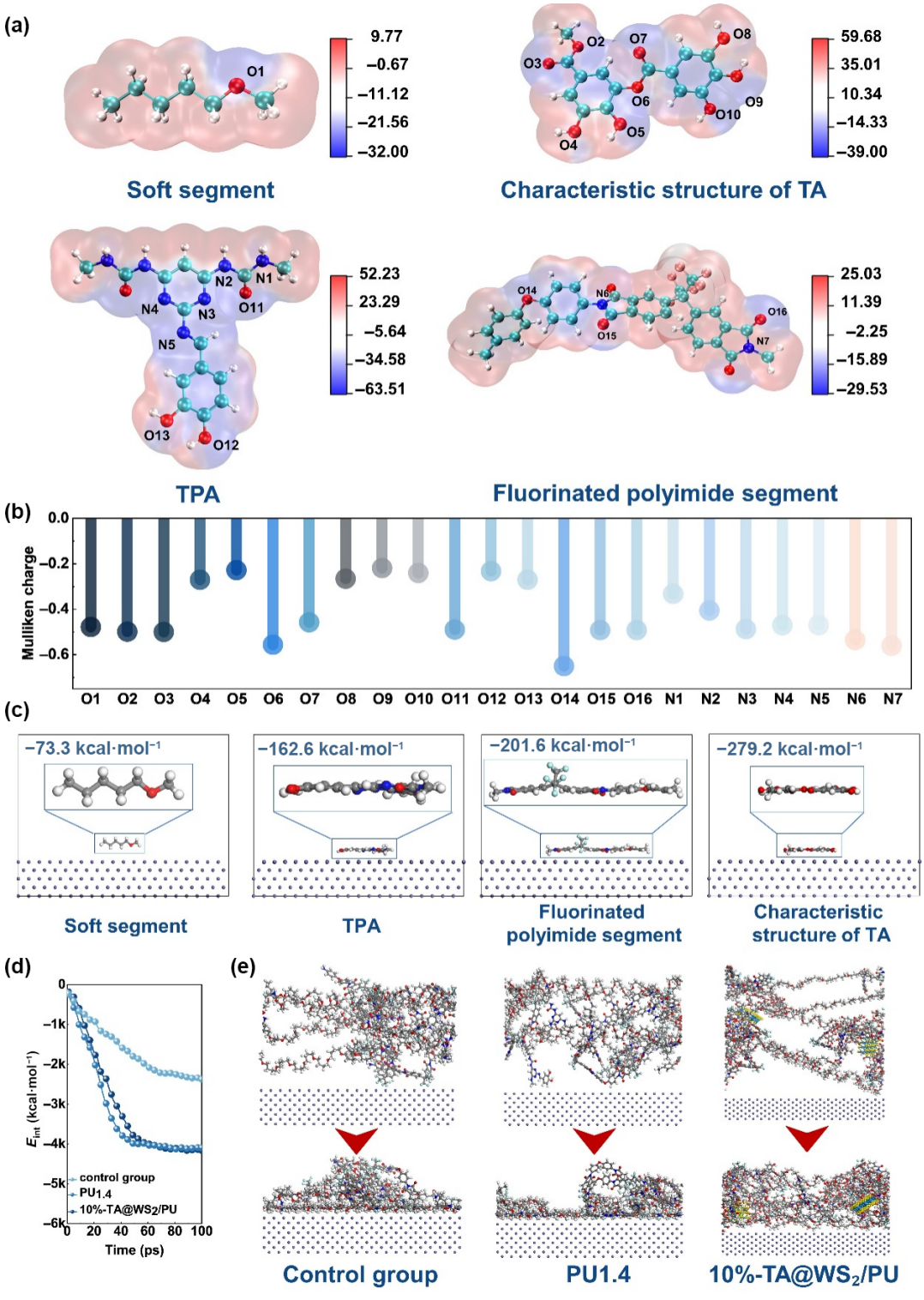

Figure 6 (a) ESP diagram of representative polar moieties of 10%-TA@WS_2/PU. (b) Mulliken atomic charges of representative polar moieties of 10%-TA@WS_2/PU. (c) Adsorption energy of representative polar moieties of 10%-TA@WS_2/PU on Fe substrate. (d) Interfacial binding energy of 10%-TA@WS_2/PU, PU1.4, and control group (replacing TPA with phenylenediamine) on Fe substrate. (e) Simulation of dynamic adsorption processes of 10%-TA@WS_2/PU, PU1.4, and control group (replacing TPA with phenylenediamine) on Fe substrate.

fluorinated polyimide segments alone, leading to a pronounced decrease in adhesion strength. Taken together, these results indicate that the strong adhesion of 10%-TA@WS_2/PU originates primarily from the cooperative interfacial adsorption of catechol-containing TPA and fluorinated polyimide segments, while the mobile soft segments further reinforce adhesion by enabling intimate surface conformity and mechanical interlocking.

2.5 Underwater adhesion properties of TA@WS_2/PU

To assess the underwater adhesive performance of 10%-

TA@WS_2/PU, the hot-melt adhesive (after preparation, 10%-TA@WS_2/PU can be thermally softened and applied as a hot-melt adhesive without requiring prolonged oven treatment during actual bonding) was first deposited onto a substrate fully immersed in water, after which a second substrate was immediately pressed against the adhesive layer under water. The lap-shear strength increased progressively with increasing pressing time and eventually leveled off at 9 min, reaching a maximum value of 4.2 MPa (Fig. 7(a)). This result indicates that underwater adhesion formation is not instantaneous, but rather involves a time-dependent interfacial reorganization process. In other words, effective underwater bonding requires sufficient time for the removal of interfacial water, the establishment of intimate contact with the substrate, and the development of strong interfacial interactions. The excellent underwater adhesion of 10%-TA@WS_2/PU was further demonstrated by its ability to lift a 2 kg steel block in a submerged state (Fig. 7(d) and Movie S2 in the ESM), confirming its strong load-bearing capacity under water. In addition, as shown in Movie S3 in the ESM, an *in situ* sealing experiment was carried out on a plastic bottle containing a 0.5 cm diameter hole while water was being sprayed. Upon pressing 10%-TA@WS_2/PU onto the damaged area, the hole was rapidly sealed and water leakage was effectively suppressed, highlighting the promise of 10%-TA@WS_2/PU for waterproof bonding and sealing applications. It is worth noting that 10%-TA@WS_2/PU exhibits excellent dry and underwater adhesion properties, far surpassing those of adhesives reported in the Refs.[14, 22, 44, 48, 51, 56–65] (Fig. 7(c)) . By comparison, PU1.4 also exhibits excellent underwater adhesion strength (3.8 MPa), but its fracture energy is significantly lower than that of 10%-TA@WS_2/PU (Fig. 7(b)). To further evaluate the environmental adaptability of 10%-TA@WS_2/PU under marine-relevant aqueous conditions, underwater adhesion tests were conducted in 3.5 wt.% NaCl solution, under hydrodynamic disturbance, and in a simulated low-temperature saline environment (Fig. S37 in the ESM). The adhesive maintained effective bonding in 3.5 wt.% NaCl solution and under the investigated fluid disturbance, indicating that its underwater adhesion is not limited to static deionized water. Under low-temperature saline conditions, however, the underwater lap-shear strength decreased to 2.14 MPa. This reduction is mainly attributed to the hot-melt nature of the adhesive: Rapid cooling and solidification at low temperature shorten the time available for spreading, interfacial water displacement, and intimate substrate contact, thereby reducing bonding efficiency.

To gain mechanistic insight into the underwater adhesion behavior, MD simulations were conducted using a ternary Fe substrate–hydration layer–10%-TA@WS_2/PU model. After equilibration, part of the hydration layer initially adsorbed on the Fe surface was displaced by 10%-TA@WS_2/PU chains (Fig. 7(e)), revealing the strong dewetting ability of the adhesive. This conclusion is further supported by the number-density profiles of water molecules along the direction from the Fe substrate toward the vacuum region (Fig. 7(f)), which show that the water content decreases markedly near the substrate surface. These results demonstrate that the original Fe-water interface is gradually replaced by an Fe-polymer interface, indicating that 10%-TA@WS_2/PU can effectively disrupt the strongly bound hydration layer on the metal surface, a key prerequisite for underwater adhesion. In-depth analysis of XPS measurements further uncovered an obvious surface feature in 10%-TA@WS_2/PU. For nitrogen atom, when the lone pair of electrons on a nitrogen atom acts as a donor in hydrogen bonding, the density of the electron cloud around the nitrogen atom decreases, thereby weakening the screening effect and increasing the binding energy of the 1s electron. Consequently, peaks with high binding energy represent the hydrogen-bonded component (blue), whilst those with low binding energy represent the non-hydrogen-bonded component (yellow). Notably, in the N 1s spectra, the surface region contains a substantially higher fraction of free N–H than the bulk interior (Fig. 7(g)), suggesting an enrichment of TPA-associated groups at the outermost surface. Meanwhile, fluorine was also found to be significantly concentrated in the surface layer (Fig. S38 in the ESM). The above results indicate that 10%-TA@WS_2/PU tends to expose both unbound catechol moieties and low-surface-energy fluorinated groups at the interface. Such a surface molecular configuration is particularly advantageous for underwater adhesion: The fluorinated groups promote water displacement from the substrate surface, while the exposed adhesive catechol groups subsequently facilitate anchoring to the substrate once the hydration barrier has been disrupted. The stability of the bonded interface under water was further examined by molecular dynamics simulations based on an Fe substrate–10%-TA@WS_2/PU–water-layer model. After 200 ps of simulation, water molecules rapidly arranged into a hydration layer at the outer surface, while no noticeable infiltration into the interior of the polymer was observed (Figs. 7(h) and 7(i)), indicating that 10%-TA@WS_2/PU is inherently capable of blocking water ingress once the adhesive interface has been formed. This interpretation is further corroborated by *in-situ* Raman characterization of the bonding interface after immersion for 24 h (Fig. 7(j)). For the control group (only with TPA)/glass interface, a clear water-related Raman band was detected, whereas no discernible water signal appeared at the 10%-TA@WS_2/PU /glass interface, demonstrating that 10%-TA@WS_2/PU can effectively suppress water accumulation within the bonded interfacial region. Combined with its previously identified low water diffusivity, strengthened microphase-separated structure, and increased cohesive energy density, these findings suggest that the exceptional underwater adhesion of 10%-TA@WS_2/PU arises from the cooperative effect of efficient interfacial dewetting, exposed adhesive groups for substrate binding, and a compact polymer matrix that resists water penetration.

Moreover, to further assess the long-term interfacial stability of 10%-TA@WS_2/PU under aqueous exposure, its adhesion retention after immersion for different durations was compared with that of PU1.4. Although PU1.4 exhibited a lap-shear strength comparable to that of 10%-TA@WS_2/PU at the initial stage of immersion, their durability diverged markedly upon prolonged water exposure. After 7 days of immersion, the lap-shear strength of 10%-TA@WS_2/PU decreased by only ~ 10%, whereas PU1.4 suffered a much larger reduction of nearly 35% (Fig. 7(k)). These results indicate that, while both materials are capable of forming underwater adhesion, 10%-TA@WS_2/PU is considerably more effective at preserving interfacial integrity during long-term service in water. This advantage is further corroborated by electrochemical impedance spectroscopy (EIS). After immersion in NaCl solution for 7 days, the low-frequency impedance modulus of 10%-TA@WS_2/PU remained essentially unchanged, whereas that of PU1.4 decreased by nearly 2 orders of magnitude (Figs. 7(l) and 7(m)). Such a sharp contrast indicates that water molecules and ionic species can penetrate the PU1.4 adhesive layer and interfacial region much

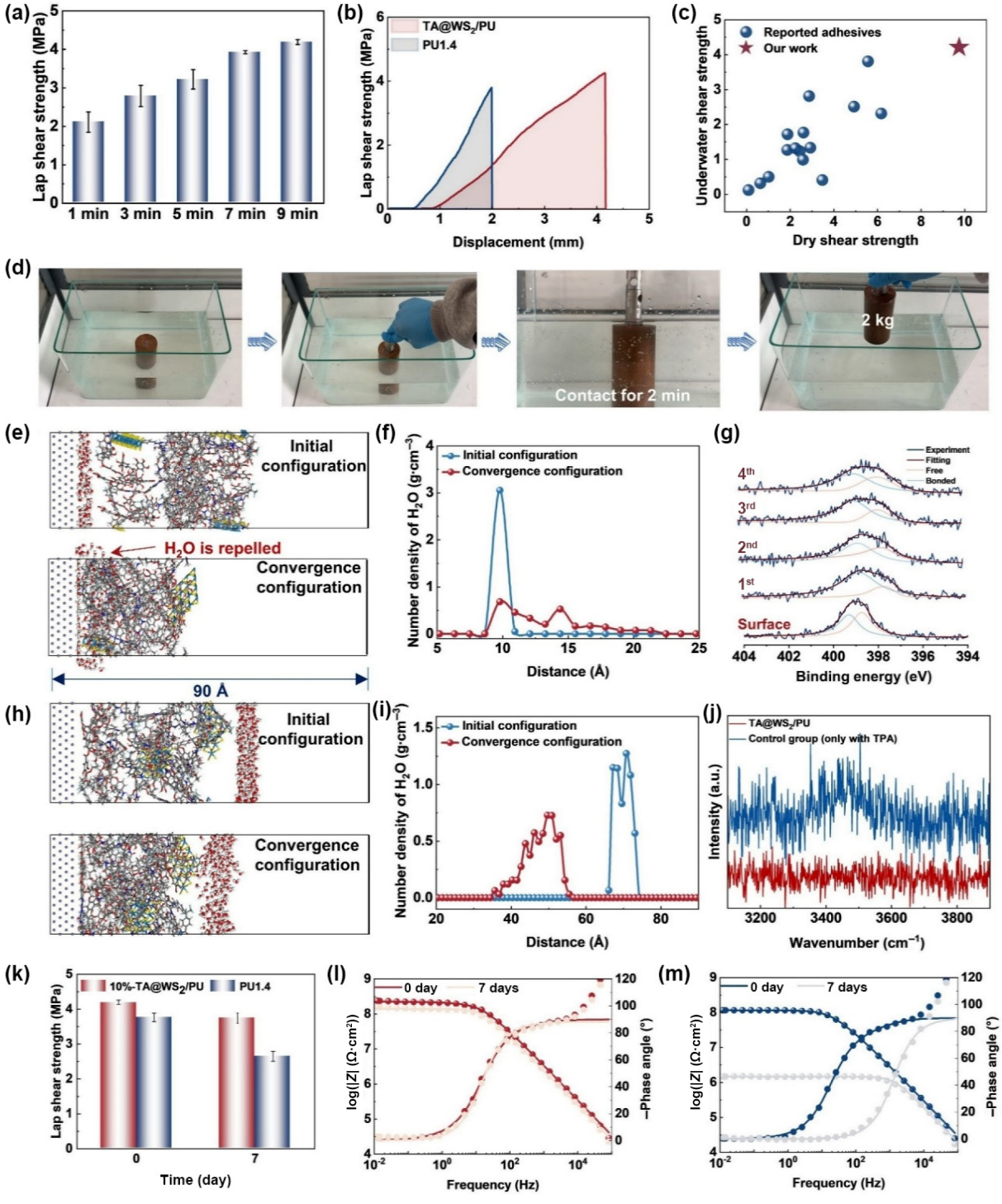

Figure 7 (a) The lap shear strength of 10%-TA@WS_2/PU after being stabilized underwater for different durations. (b) The lap shear strength of 10%-TA@WS_2/PU and PU1.4. (c) Comparison of dry and underwater lap shear strength between 10%-TA@WS_2/PU and adhesives reported. (d) Digital photos of 10%-TA@WS_2/PU underwater adhesion. (e) Molecular dynamics simulation plot of the Fe substrate–hydration layer–10%-TA@WS_2/PU system and (f) its water molecular number density. (g) XPS spectrum of the N 1s region of the adhesive surface and the material interior of 10%-TA@WS_2/PU. (h) Molecular dynamics simulation plot of the Fe substrate–10%-TA@WS_2/PU system–hydration layer and (i) its water molecular number density. (j) Underwater Raman spectra of 10%-TA@WS_2/PU and control group (only with TPA). (k) The lap shear strength of 10%-TA@WS_2/PU and PU1.4 after being immersed in water for different durations. Bode plots of (l) 10%-TA@WS_2/PU and (m) PU1.4 after immersion in 3.5 wt.% NaCl solution for varying durations.

more readily, thereby weakening its barrier function and accelerating interfacial degradation. By contrast, the superior stability of 10%-TA@WS_2/PU can be attributed primarily to the barrier effect introduced by TA@WS_2. The high-aspect-ratio nanosheets create a more tortuous diffusion pathway for water and corrosive species, thereby retarding their transport through the adhesive layer. Meanwhile, tannic-acid modification improves the interfacial compatibility between WS_2 and the polyurethane matrix,

promoting a denser and more continuous internal structure with fewer defect-mediated transport channels. Together, these effects endow 10%-TA@WS_2/PU with a more robust water-resistant interfacial architecture, enabling sustained adhesion stability under prolonged aqueous conditions.

3 Conclusions

In this study, we proposed a dual-bioinspired strategy to develop a strong, tough, durable, and recyclable amphibious adhesive by integrating the hydrophobic–hydrophilic adhesion mechanism of barnacle cement proteins with the fibre-reinforced load-bearing structure of articular cartilage. The catechol-containing chain extender provided abundant interfacial anchoring sites, while the fluorinated polyimide segments induced pronounced microphase separation and generated low-surface-energy hydrophobic nanodomains, enabling efficient disruption of hydration layers and stable interfacial contact under water. Meanwhile, tannic-acid-modified WS_2 nanosheets were incorporated into the optimized PU1.4 matrix to construct a cartilage-mimetic reinforcing network. Owing to the strong matrix–filler coupling and nanosheet-mediated energy dissipation, the resulting 10%-TA@WS_2/PU exhibited a tensile strength of 108 MPa, elongation at break of 1150%, and toughness of 371 MJ·m^{-3}, together with a high dry lap-shear strength of 9.6 MPa on Fe substrates. More importantly, 10%-TA@WS_2/PU achieved an underwater lap-shear strength of 4.2 MPa and maintained excellent adhesion stability during prolonged aqueous exposure. The incorporation of TA@WS_2 markedly enhanced environmental durability: after 7 days of immersion in water, HCl solution, and NaOH solution, 10%-TA@WS_2/PU showed only 3.0%, 8.3%, and 13.0% decreases in tensile strength, respectively. Its lap-shear strength remained above 7.5 MPa after 24 h exposure to these media and decreased by only 16% after 9 days in water. In addition, 10%-TA@WS_2/PU retained over 83% of its original adhesion strength at 100 °C and maintained high bonding strength after 1 day of hot-water immersion, demonstrating excellent thermal and hydrothermal stability. It is worth noting that 10%-TA@WS_2/PU also showed excellent repeatability and recyclability, maintaining > 90% adhesion strength after 10 rebonding cycles and ~ 100% lap-shear strength after five dissolution–reprocessing cycles. This work provides a promising molecular and structural design strategy for developing high-performance amphibious adhesives for marine repair, wet-environment sealing, and sustainable adhesive applications.

Electronic Supplementary Material: Supplementary material (detailed synthesis procedures, structural characterization, mechanical and adhesion testing, and molecular simulations, providing experimental and theoretical insights into the mechanical performance, environmental stability, and adhesion mechanisms of the bioinspired amphibious adhesives) is available in the online version of this article at https://doi.org/10.26599/NR.2026.94909211.

Data availability

All data needed to support the conclusions in the paper are presented in the manuscript and the Electronic Supplementary Material. Additional data related to this paper may be requested from the corresponding author upon request.

Acknowledgements

Financial support for this work was provided by the National Natural Science Foundation of China (No. 52435004), the China Postdoctoral Science Foundation (No. 2025M771365), the Fundamental Research Funds for the Central Universities (No. 2682025CX039), the Sichuan Science and Technology Program (Nos. 2025ZYD0038 and 2026NSFSC1237), the Opening Project of Material Corrosion and Protection Key Laboratory of Sichuan province (No. 2025CL02), the Shandong Provincial Natural Science Foundation (No. ZR2026QC0457), Opening Project of the Key Laboratory of Bionic Engineering (Ministry of Education), Jilin University (No. KF202604), and the 111 Project (No. B20008).

Declaration of competing interest

The authors declare no competing financial interest.

Author contribution statement

W. T.: Data curation, project administration, validation, writing manuscript, experimental design. J. J. D.: Data curation, project administration, validation, experimental design. J. Z.: Funding acquisition. Z. R. Z.: Project administration.

Use of AI statement

During the preparation of this work, the authors used DeepSeek for language polishing.

References

[1] Cui, C. Y.; Liu, W. G. Recent advances in wet adhesives: Adhesion mechanism, design principle and applications. *Prog. Polym. Sci.* **2021**, *116*, 101388.

[2] Wu, S. J.; Zhao, X. H. Bioadhesive technology platforms. *Chem. Rev.* **2023**, *123*, 14084–14118.

[3] Huang, P.; Zhang, H. J.; Zeng, H. B. Mussel-inspired molecular strategies for fabricating functional materials with underwater adhesion and self-healing properties. *Adv. Mater.* **2025**, *37*, 2501542.

[4] Qin, C. X.; Ma, Y. F.; Zhang, Z. Z.; Du, Y. J.; Duan, S. D.; Ma, S. H.; Pei, X. W.; Yu, B.; Cai, M. R.; He, X. M. et al. Water-assisted strong underwater adhesion via interfacial water removal and self-adaptive gelation. *Proc. Natl. Acad. Sci. USA* **2023**, *120*, e2301364120.

[5] Yao, L.; Lin, C. J.; Duan, X. Z.; Ming, X. Q.; Chen, Z. X.; Zhu, H.; Zhu, S. P.; Zhang, Q. Autonomous underwater adhesion driven by water-induced interfacial rearrangement. *Nat. Commun.* **2023**, *14*, 6563.

[6] Cheng, B. H.; Yu, J. H.; Arisawa, T.; Hayashi, K.; Richardson, J. J.; Shibuta, Y.; Ejima, H. Ultrastrong underwater adhesion on diverse substrates using non-canonical phenolic groups. *Nat. Commun.* **2022**, *13*, 1892.

[7] Shi, C. Y.; He, D. D.; Zhang, Q.; Tong, F.; Shi, Z. T.; Tian, H.; Qu, D. H. Robust and dynamic underwater adhesives enabled by catechol-functionalized poly(disulfides) network. *Natl. Sci. Rev.* **2023**, *10*, nwac139.

[8] Abe, H.; Yoshihara, D.; Tottori, S.; Nishizawa, M. Mussel-inspired thermo-switchable underwater adhesive based on a Janus hydrogel. *NPG Asia Mater.* **2024**, *16*, 49.

[9] Zheng, S. Y.; Zhou, J. H.; Wang, S. B.; Wang, Y. J.; Liu, S. Q.; Du, G. Y.; Zhang, D.; Fu, J. M.; Lin, J.; Wu, Z. L. et al. Water-triggered spontaneously solidified adhesive: From instant and strong underwater adhesion to *in situ* signal transmission. *Adv. Funct. Mater.* **2022**, *32*, 2205597.

[10] Su, X.; Xie, W. Y.; Wang, P. D.; Tian, Z. L.; Wang, H.; Yuan, Z. Y.; Liu, X. Z.; Huang, J. Y. Strong underwater adhesion of injectable hydrogels triggered by diffusion of small molecules. *Mater. Horiz.* **2021**, *8*, 2199–2207.
[11] Gan, K. S.; Liang, C.; Bi, X. Y.; Wu, J. Z.; Ye, Z. H.; Wu, W. J.; Hu, B. R. Adhesive materials inspired by barnacle underwater adhesion: Biological principles and biomimetic designs. *Front. Bioeng. Biotechnol.* **2022**, *10*, 870445.
[12] Wang, Z.; Zhang, S. F.; Zhao, S. J.; Kang, H. J.; Wang, Z. K.; Xia, C. L.; Yu, Y. L.; Li, J. Z. Facile biomimetic self-coacervation of tannic acid and polycation: Tough and wide pH range of underwater adhesives. *Chem. Eng. J.* **2021**, *404*, 127069.
[13] Liu, Y. C.; Li, K.; Tian, J. H.; Gao, A. T.; Tian, L. H.; Su, H.; Miao, S. T.; Tao, F.; Ren, H.; Yang, Q. M. et al. Synthesis of robust underwater glues from common proteins via unfolding-aggregating strategy. *Nat. Commun.* **2023**, *14*, 5145.
[14] Yang, H. L.; Wang, W. Q.; Zhu, C. J.; Chen, G. Q.; Zheng, J. X.; Li, S. N.; Ren, J. Y.; Fu, J. Reversible, ultra-strong underwater adhesive based on supramolecular interaction for instant liquid leakage sealing and robust tissue adhesion. *Chem. Eng. J.* **2024**, *480*, 148064.
[15] Wang, S. X.; Waite, J. H. Catechol redox maintenance in mussel adhesion. *Nat. Rev. Chem.* **2025**, *9*, 159–172.
[16] Lu, Z.; Bai, S. Y.; Lu, H.; Zhu, Z. H.; Yu, J.; Wang, Q.; Zhang, P.; Qian, L.; Zheng, Z. J.; Yu, Y. Rapid photocontrollable dopamine polymerization for instant adaptive wet adhesion. *Nat. Commun.* **2026**, *16*, 11150.
[17] Peng, H.; Zhang, Z. T.; Khare, V.; Das, A. A.; Razaviamri, F.; Wang, K.; Lee, B. P. Electrochemical deactivation of high-strength, catechol-based adhesives incorporated with anhydrous proton and electron conducting elements. *Commun. Mater.* **2026**, *7*, 114.
[18] Li, Y. H.; Liu, Z. Y.; Wang, T. C.; Wang, M. L.; Yao, H. R.; Gao, F.; Cheng, J.; Zhang, J. Y. Barnacle-inspired amphipathic high strength adhesives under-water/oil. *Chem. Eng. J.* **2024**, *498*, 155067.
[19] Zhang, Y. N.; Zhao, Z. H.; Wang, L.; Sun, F. Y.; Xu, J. H.; Yao, B. W.; Sun, Z.; Liu, T.; Zeng, Y. H.; Zhang, G. P. et al. Barnacle-inspired underwater adhesive with instant, robust, and reversible adhesion on diverse surfaces. *Adv. Funct. Mater.* **2025**, *35*, e07942.
[20] Gao, X.; Fang, X.; Wang, H.; Tian, N. A.; Sun, J. Q. Fully erasable amphibious adhesives derived from soybean oil with record-high underwater adhesion strength. *Adv. Mater.* **2025**, *37*, e07894.
[21] Li, M.; Wu, X. K.; Chen, X. L.; Li, H. N.; Xiong, P. F.; Zhao, S. J.; Wang, Z. K.; Wang, Z. A hydrophobic phase-locking strategy enabling ultrarobust and water-stable self-healing elastomers for underwater ionotronics. *Chem. Eng. J.* **2024**, *498*, 155253.
[22] Wu, X. K.; Li, M.; Li, H. A.; Gao, H. H.; Wang, Z. K.; Wang, Z. Autonomous underwater self-healable adhesive elastomers enabled by dynamical hydrophobic phase-separated microdomains. *Small* **2024**, *20*, 2311131.
[23] Wilson, M. C.; Beasley, M. A.; Fears, K. P.; Yates, E. A.; So, C. R. Role of protein aggregate structure on the strength and underwater performance of barnacle-inspired adhesives. *Soft Matter* **2023**, *19*, 4254–4264.
[24] Wu, F. L.; Han, S. H.; Hu, X. P.; Deng, C. Barnacle-inspired robust adhesive strategy integrating with surface topological engineering for durable fire protection of polyurethane foam. *Chem. Eng. J.* **2025**, *525*, 170428.
[25] Nogusa, T.; Cooper, C. B.; Yu, Z. A.; Zheng, Y.; Shi, Y. R.; Bao, Z. A. Tunable, reusable, and recyclable perfluoropolyether periodic dynamic polymers with high underwater adhesion strength. *Matter* **2023**, *6*, 2439–2453.
[26] Han, L.; Wang, M. H.; Prieto-López, L. O.; Deng, X.; Cui, J. X. Self-hydrophobization in a dynamic hydrogel for creating nonspecific repeatable underwater adhesion. *Adv. Funct. Mater.* **2020**, *30*, 1907064.
[27] Li, X. Q.; Cheng, N. B.; Lin, Y. Y.; Zhang, B.; Yang, Y. Z.; Qu, C. R.; Wang, X. F.; Yu, J. Y.; Ding, B. Articular cartilage inspired ultra-strong and tough bio-based polyurethane nanofiber membranes. *Angew. Chem., Int. Ed.* **2025**, *64*, e202505034.
[28] Wang, Y. Y.; Huang, X.; Zhang, X. X. Ultrarobust, tough and highly stretchable self-healing materials based on cartilage-inspired noncovalent assembly nanostructure. *Nat. Commun.* **2021**, *12*, 1291.
[29] Tian, W.; Deng, J. J.; Zheng, J.; Zhou, Z. R. A thermosetting elastomer coating induced by imperfect matching with high toughness, high adhesion strength, and recyclability. *Prog. Org. Coat.* **2026**, *213*, 109918.
[30] Tian, W.; Deng, J. J.; Zheng, J.; Zhou, Z. R. Fabrication of water-resistant and high-temperature-tolerant adhesives through synergistic bionic strategy to achieve balanced adhesion and cohesion. *J. Colloid Interface Sci.* **2026**, *707*, 139705.
[31] Tian, W.; Guo, Z. L.; Wang, S. L.; Yu, H. T.; Wang, S.; Jin, H. C.; Tian, L. M. Hydrogen and DA bond-based self-healing epoxy-modified polyurea composite coating with anti-cavitation, anticorrosion, antifouling, and strong adhesion properties. *J. Mater. Sci. Technol.* **2024**, *187*, 1–14.
[32] Tian, W.; Deng, J. J.; Wang, H. J.; Zheng, J.; Zhou, Z. R. A Hierarchical energy dissipation supramolecular elastomer with superhigh toughness and cohesive strength for adhesive applications. *Macromolecules* **2026**, *59*, 298–311.
[33] Bai, Z. C.; Li, X. D.; Wu, T. H.; Jiang, H.; Zhang, X. D.; Zhang, L. C.; Yang, Y.; Liu, S.; Lei, L. S.; Song, N. N. et al. A facile and on-demand optimizing strategy for polyurethane elastomers via programmable hydrogen bonding. *Chem. Eng. J.* **2024**, *492*, 152110.
[34] He, L.; Wei, J. L.; Ren, Z. Q.; Li, Y. X.; Zhang, Z. B.; Li, G. F.; Huang, F. H.; Li, S. J. Polyurethane elastomers strengthened by pseudo[1]rotaxanes based on pillararenes. *Angew. Chem., Int. Ed.* **2025**, *64*, e202421557.
[35] Li, Y. W.; Peng, S. Q.; Kankala, R. K.; Wu, L. X.; Chen, A. Z.; Wang, S. B. 3D printing of mechanically robust MXene-encapsulated polyurethane elastomer. *Compos. Part A: Appl. Sci. Manuf.* **2022**, *163*, 107182.
[36] Luo, K. L.; Wang, X. Y.; Dou, Q.; Cao, P. R.; Yang, J.; Guo, L. H.; Guo, Q.; Li, S.; Wang, Q. H.; Wang, T. M. et al. Engineering of chain extender flexibility and hierarchical hydrogen bonding toward ultra-low-temperature poly(urethane-urea) elastomers with exceptional toughness. *Small* **2025**, *21*, e09686.
[37] Luo, Y. L.; Chen, J. L.; Situ, G. H.; Li, C. C.; Zhang, C. R.; Li, F. Z.; Li, C. H.; Luo, Z. Y.; Zhang, X. Aromatic disulfide-induced self-reinforcing polyurethane elastomer with self-healability. *Chem. Eng. J.* **2023**, *469*, 143958.
[38] Shi, J. X.; Zheng, T. Z.; Wang, Z. Q.; Wang, P. J.; Yang, H. K.; Guo, J. J.; Wang, D.; Guo, B. H.; Xu, J. Filler effects inspired high performance polyurethane elastomer design: Segment arrangement control. *Mater. Horiz.* **2024**, *11*, 4747–4758.
[39] Wang, C. Y.; Ma, K.; Wang, X. X.; Chen, K. Z.; Qiao, S. L. Mechanical robust and recyclable PLA-based polyurethane elastomers for flexible electronics. *Chem. Eng. J.* **2025**, *522*, 167855.
[40] Wu, X. K.; Zhang, J. L.; Li, H. N.; Gao, H. H.; Wu, M.; Wang, Z. K.; Wang, Z. Dual-hard phase structures make mechanically tough and autonomous self-healable polyurethane elastomers. *Chem. Eng. J.* **2023**, *454*, 140268.
[41] Yao, W. J.; Li, J. Y.; Wei, C.; Liu, D. S.; Liu, W.; Ma, J. H.; He, Z. R.; Li, Z. J.; Tian, Q. Y.; Guo, K. et al. Photothermally triggered self-healing polyurethane elastomers for multifunctional thermochromic fluorescence devices. *Adv. Funct. Mater.* **2026**, *36*, e31865.
[42] Zhou, Y.; Jiang, X.; Yang, X. L.; Liang, H.; Xie, X.; Fu, W. L. Self-lubricating and self-healing polyurethane elastomer as a meniscal prosthesis to delay osteoarthritis progression. *Adv. Funct. Mater.* **2025**, *35*, 2420344.
[43] Huang, Z.; Geng, S. M.; Chen, Y. Z.; Li, Y.; Fei, M. E.; Qiu, R. H.; Chen, T. T.; Liu, W. D. Biobased comb polyurethane hot-melt adhesives consisting of dangling fatty acid chains and H-bonds for tailoring bonding strength. *Eur. Polym. J.* **2025**, *229*, 113880.

[44] Pu, M. Y.; Fang, C. Q.; Zhou, X.; Wang, X. P.; Yang, M. N.; Su, J.; Tang, X. Y.; Chen, Y. R.; Shang, Y. J. Dopamine-grafted polyurethane adhesives derived from glycolyzed PET: Toward sustainable and high-performance underwater bonding. *Chem. Eng. J.* **2026**, *530*, 173303.

[45] Huang, Z. S.; Qin, C.; Guo, H. X.; Yuan, H.; Cao, Y. Z.; Wang, Z.; Jin, C. D. Environmental-friendly bio-based thermosetting non-isocyanate polyurethane adhesive with enhanced bonding strength. *J. Clean. Prod.* **2025**, *520*, 146076.

[46] Lechuga-Islas, V. D.; Gillissen, E.; Bourguignon, M.; Grignard, B.; Detrembleur, C. Foam-to-adhesive recycling of self-blown non-isocyanate polyurethane foams facilitated by integration of disulfide exchangeable bonds and moisture. *Chem. Eng. J.* **2025**, *516*, 163998.

[47] Türel, T.; Cristadoro, A. M.; Linnenbrink, M.; Tomović, Ž. Harnessing imine chemistry for the debonding-on-demand of polyurethane adhesives. *ACS Appl. Mater. Interfaces* **2025**, *17*, 2656–2665.

[48] Yang, R.; Tan, L.; Pan, Z.; Tian, L. F.; Zhang, T. C.; Zhao, B. Z.; Song, F.; Zhou, Y. H.; Zhang, M. High strength, self-activating ability and fast adhesion of polyurethane adhesives based on rosin structure in different environments. *Mater. Horiz.* **2025**, *12*, 1913–1921.

[49] Danielson, M. K.; Sumpter, B. G.; Demchuk, Z.; Gainaru, C.; Pan, C. Y.; Saito, T.; Rahman, M. A. High-performance reversible adhesive from PET waste for underwater, structural, and pressure-sensitive applications. *Sci. Adv.* **2025**, *11*, eadw1288.

[50] Zhao, X. H.; Ding, J. J.; Xuan, C. K.; Liao, J. N.; Shi, X. T. High-strength bone polyurethane adhesive with rapid curing for bone tissue injury repair. *J. Mater. Chem. B* **2025**, *13*, 5150–5162.

[51] Dai, S. P.; He, J. X.; Yao, J. P.; Zou, J. X.; Ye, H. X.; Pan, C. W.; Guo, T. P.; Chen, W. T.; Sui, Y. Novel tripodal cross-linker-mediated supramolecular 3D network polyurethanes: Superior adhesion properties and underwater applications. *Chem. Eng. J.* **2025**, *524*, 169810.

[52] Restrepo-Montoya, A. C.; Bernaerts, K. V.; Eceiza, A.; Saralegi, A. Recyclable thermoset polyurethane adhesives based on thermoreversible DA-adducts for wood and metal substrates. *J. Clean. Prod.* **2026**, *556*, 148209.

[53] Wang, S. L.; Liu, Z. H.; Zhang, L. Z.; Guo, Y. F.; Song, J. C.; Lou, J. M.; Guan, Q. B.; He, C. L.; You, Z. W. Strong, detachable, and self-healing dynamic crosslinked hot melt polyurethane adhesive. *Mater. Chem. Front.* **2019**, *3*, 1833–1839.

[54] Liu, H. Z.; Cao, S. T.; Liu, Z. L.; Wang, J. Y.; Liu, Y. T.; Sun, L. S.; Gao, C. H. Sulfur-modified polyurethane adhesives: Green synthesis process and disassembly-responsive characteristics. *Polym. Degrad. Stab.* **2024**, *228*, 110910.

[55] Wang, D.; Li, J. Y.; Wang, Y. K.; Omoniyi, A. O.; Fu, Z. W.; Zhang, J. F.; Su, Z. M. Water-based polyurethane adhesive films with enhanced bonding strength capable of *in situ* and high-efficient deposition on metal surface. *Chem. Eng. J.* **2022**, *431*, 134055.

[56] Guo, X. L.; Zhao, X.; Yuan, L.; Ming, H.; Li, Z.; Li, J. H.; Luo, F.; Tan, H. Bioinspired injectable polyurethane underwater adhesive with fast bonding and hemostatic properties. *Adv. Sci.* **2024**, *11*, 2308538.

[57] Liu, B. Y.; Li, Z. Y.; Zhang, J. S.; Du, M.; Fang, F.; Chen, F. S. An environment-friendly wood adhesive using modified wheat gluten by isophorone diisocyanate. *Ind. Crops Prod.* **2021**, *173*, 114125.

[58] Mao, S. H.; Zeng, G. D.; Xing, J. P.; Dong, Y. M.; Aladejana, J. T.; Chu, F. X.; Wang, C. P.; Li, J. Z. High water retention bio-mass adhesives inspired by hydrogels for engineering applications. *Ind. Crops Prod.* **2025**, *224*, 120283.

[59] Xie, X. M.; Li, R. H.; Qiao, Y. S.; Zhang, J. Q.; Zhang, Z. L.; Xu, X. Y.; Yang, J.; Peng, Y. Y.; Chen, Y. F.; Li, S. L. et al. An *in-situ* assembled cobweb-like adhesive with high processability. *Nat. Commun.* **2025**, *16*, 4872.

[60] Gomez-Lopez, A.; Grignard, B.; Calvo, I.; Detrembleur, C.; Sardon, H. Monocomponent non-isocyanate polyurethane adhesives based on a sol-gel process. *ACS Appl. Polym. Mater.* **2020**, *2*, 1839–1847.

[61] Han, Y. F.; Zhou, W. G.; Sun, X. Y.; Kong, X. M.; Li, J. Z. Mussel-inspired magnesium oxychloride cement-based wood adhesive produced via the synergy of inorganic fiber enhancement and multiple reinforcement network. *Constr. Build. Mater.* **2024**, *439*, 137391.

[62] Zhao, H. Q.; Yao, W. R.; Liu, G. Y.; Chen, K.; Liu, M. Y.; Sun, C.; Shen, J.; Tan, H. Y.; Zhang, Y. H. A new strategy for the preparation of high-strength hydrophobic aldehyde-free starch adhesive. *Polym. Adv. Technol.* **2024**, *35*, e70000.

[63] Liu, J.; Huang, W. K.; Han, Z. L.; Zang, Y.; Wang, J. J.; Tan, H.; Kong, L. P. A polyurethane underwater adhesive with strong adhesion and self-curing capability. *Eur. Polym. J.* **2025**, *239*, 114300.

[64] Zheng, G. H.; Zhang, S. T.; Wang, Y. W.; Pan, A. B.; Xu, B. K.; Xu, Y. T.; Zhang, X. C. Preparation of a multifunctional bio-based adhesive inspired by the structure of dragonfly wings. *Compos. Part B: Eng.* **2025**, *298*, 112374.

[65] Sun, Q. L.; Jiang, J. J.; Chen, K.; Zhan, J. F.; Sun, C.; Tan, H. Y.; Zhang, Y. H. A study on the preparation of high-strength starch-based adhesives with multiple cross-linked structures based on epoxy modification. *Int. J. Biol. Macromol.* **2025**, *333*, 148739.

This is an open access article under the terms of the Creative Commons Attribution 4.0 International License (CC BY 4.0, https://creativecommons.org/licenses/by/4.0/).

© The Author(s) 2027. Published by Tsinghua University Press.